

A First-Passage Kinetic Monte Carlo Method for Reaction-Drift-Diffusion Processes

Ava J. Mauro ^{*} Jon Karl Sigurdsson [†] Justin Shrake [‡] Paul J. Atzberger [§]
 Samuel A. Isaacson [¶]

Abstract

Stochastic reaction-diffusion models are now a popular tool for studying physical systems in which both the explicit diffusion of molecules and noise in the chemical reaction process play important roles. The Smoluchowski diffusion-limited reaction model (SDLR) is one of several that have been used to study biological systems. Exact realizations of the underlying stochastic process described by the SDLR model can be generated by the recently proposed First-Passage Kinetic Monte Carlo (FPKMC) method. This exactness relies on sampling analytical solutions to one and two-body diffusion equations in simplified protective domains.

In this work we extend the FPKMC to allow for drift arising from fixed, background potentials. As the corresponding Fokker-Planck equations that describe the motion of each molecule can no longer be solved analytically, we develop a hybrid method that discretizes the protective domains. The discretization is chosen so that the drift-diffusion of each molecule within its protective domain is approximated by a continuous-time random walk on a lattice. New lattices are defined dynamically as the protective domains are updated, hence we will refer to our method as Dynamic Lattice FPKMC or DL-FPKMC. We focus primarily on the one-dimensional case in this manuscript, and demonstrate the numerical convergence and accuracy of our method in this case for both smooth and discontinuous potentials. We also present applications of our method, which illustrate the impact of drift on reaction kinetics.

1 Introduction

A fundamental challenge in cell biology is to understand how to predict and control the dynamics of cellular processes [2]. Stochasticity in the quantities and movements of molecules can have significant effects on the outcomes of cellular processes, particularly given the low copy numbers of many signaling and regulatory proteins and mRNAs present in a cell. For such species, the actual number and locations of molecules can provide a more accurate and useful description than the local concentration. The method we present in this paper allows for the explicit simulation of the stochastically varying numbers and locations of molecular species undergoing chemical reactions and drift-diffusion.

Experimental studies and mathematical models have shown that stochasticity in the chemical reaction process plays a role in many cellular processes, for example gene expression [10, 19, 55], cell-fate decision making [64, 42], and signaling pathways in development [5]. Mathematical models of such processes frequently treat an individual cell as a single well-mixed volume or a small number of well-mixed compartments, such as the nucleus and the cytoplasm. However, the heterogeneous spatial distribution of chemical species, as well as interactions with internal membranes and organelles, often have significant effects on cellular processes. For example, after gene regulatory proteins enter the nucleus through nuclear pores, the time required to find specific DNA binding sites can be significantly influenced by the spatial structure of DNA within the nucleus [35]. Similarly, the spatial distribution of components of cellular signaling processes can play a decisive role in the successful propagation of signals from the cell membrane to the nucleus [46, 38].

A number of stochastic reaction-diffusion models have been introduced to understand the combined influence of noise due to the chemical reaction process and spatial diffusion [1, 18, 65, 35]. These mathematical models resolve

^{*}Department of Mathematics and Statistics, Boston University, 111 Cummington St., Boston, MA 02215 (avamauro@bu.edu)

[†]Department of Mathematics, University of California, Santa Barbara

[‡]Department of Mathematics, University of California, Santa Barbara

[§]6712 South Hall, Department of Mathematics, University of California, Santa Barbara, CA 93106 (atzberg@math.ucsb.edu)

[¶]Department of Mathematics and Statistics, Boston University, 111 Cummington St., Boston, MA 02215 (isaacson@math.bu.edu)

the explicit spatial movement of proteins and mRNAs within cells. There are three such mathematical models that have been commonly used: the spatially-continuous Smoluchowski diffusion-limited reaction model (SDLR) [61, 37]; what we call the Doi model [66, 15, 16]; and the lattice-based reaction-diffusion master equation model (RDME) [24, 43].

These models often treat the movement of molecules as purely diffusive; however, drift can also play a significant role in the dynamics of cellular processes. Examples of sources of such drift include active transport, variations in chemical potential, material heterogeneities in the cytoplasm and nucleoplasm, and local interactions with cellular structures. The incorporation of drift has played a key role in developing models for molecular-motor based active transport [50, 6], movement of proteins on DNA [60], and protein movement subject to the influence of volume exclusion by chromatin [35]. It has been shown how to extend the RDME to incorporate drift due to potentials [35]. In the present work we consider a generalization of the SDLR model that allows for drift due to fixed potentials. For creating realizations of the stochastic process described by this model, we present a new numerical method, combining elements of the First-Passage Kinetic Monte Carlo (FPKMC) method [48, 47, 17, 65] and the lattice methods of [70, 35]. We will refer to our method as Dynamic Lattice FPKMC or DL-FPKMC.

1.1 The SDLR and RDME Models

In this subsection we compare the SDLR and RDME models to provide motivation for our choice of the SDLR model. In the standard SDLR approach [61], the positions of molecules are modeled as point particles undergoing Brownian motion. The state of a chemical system is given by the collection of stochastic processes for the positions of each molecule of each chemical species at a given time. Bimolecular, or second-order, reactions between two molecules are modeled as occurring either instantaneously, or with an intrinsic reaction-rate, when the molecules' separation reaches a specified reaction radius [37]. Bimolecular reactants are not allowed to approach closer than their reaction radius. Unimolecular, or first-order, reactions involving a single molecule represent internal processes, such as decay or splitting, and are assumed to occur with specified probabilities per unit time. (The Doi model is similar, but allows bimolecular reactants to approach arbitrarily close to each other. Bimolecular reactions then occur with a fixed probability per unit time when the separation between two molecules is *less than* the reaction-radius [66, 15, 16].) The SDLR model can be extended to incorporate drift due to potentials. The underlying reaction process remains unchanged, but molecules move by a drift-diffusion process instead of pure Brownian motion. We give a more detailed description of the SDLR model with drift in Section 2, where we also discuss the different bimolecular reaction mechanisms and where reaction products should be placed.

In contrast to the spatially-continuous SDLR model, space in the RDME is partitioned by a mesh into a collection of voxels. The diffusion of molecules is approximated by a continuous-time random walk on the mesh, with bimolecular reactions occurring with a fixed probability per unit time for molecules within the same voxel. Unimolecular reactions are modeled in the same manner as in the SDLR model. The state of a chemical system is then described by the collection of stochastic processes for the number of each chemical species within each voxel at a given time. Molecules are assumed to be well-mixed within each voxel (i.e. uniformly distributed). The RDME can be considered an extension of the chemical master equation (CME), a standard non-spatial model for stochastic chemical kinetics [24, 43, 23, 68, 53]. One advantage of the RDME is the ability to construct a hierarchy of more macroscopic approximations for which efficient numerical solution methods have been developed [57].

When the RDME is interpreted as an independent physical model [21, 54] there is a nonzero, lower bound on the lattice spacing that arises from the assumption that the diffusive mixing timescale within a voxel is faster than the timescale for a (well-mixed) bimolecular reaction to occur [36, 22]. There is also a simultaneous upper bound on the lattice spacing to ensure the random walk approximation of molecular diffusion is accurate. Only when these bounds are both satisfied is the RDME considered "physically valid". However, in the absence of nonlinear reactions, the solution to the RDME should *converge* to that of the SDLR model. This can be seen by considering the particle-tracking representation of the RDME derived in [31]. It is also standard to choose the diffusive hopping rates in the RDME so that, in the absence of any reactions, the solution to the RDME recovers the Brownian motion of point particles as the lattice spacing is taken to zero [36, 20]. For these reasons, in applications the RDME is often considered an approximation to the more microscopic SDLR model [54, 22, 28].

For systems that include bimolecular reactions, interpreting the RDME as an approximation to the SDLR model can be problematic. It has been proven that in the continuum limit that the RDME lattice spacing is taken to zero bimolecular reactions are lost in two or more dimensions [32, 34, 28]. As such, the time required for two molecules to react becomes infinite. The loss of bimolecular reactions is consistent with the physical lower bound on the lattice

spacing, and demonstrates that the RDME can only be interpreted as an approximation to the SDLR model for lattice spacings that are neither too large nor too small. The error of this approximation cannot be made arbitrarily small. In [34] the two molecule $A + B \rightarrow \emptyset$ reaction was studied in \mathbb{R}^3 in both the RDME and SDLR model. It was shown that for certain biologically relevant parameter values the reaction time distribution in the RDME could *at best* approximate the reaction time distribution in the SDLR model to within 5-10% percent for an optimal choice of lattice spacing.

Several recent efforts have derived renormalized bimolecular reaction rates for use in the RDME that are designed to accurately capture *one specific statistic* of the SDLR model over a range of sufficiently large lattice spacings [22, 28]. For example, [22] matches the mean equilibration time for the $A + B \rightleftharpoons C$ reaction in a system with one A molecule and one B molecule. More recently, a modified convergent RDME (CRDME) that approximates the Doi model was proposed in [33]. Still, as of yet there is no RDME-like approximation of the (microscopic) SDLR model in which the approximation error can be made arbitrarily small.

There are several additional challenges to using RDME-like lattice models to study cellular processes in realistic geometries. Foremost, existing methods for formulating RDMEs approximate the domain geometry by either unstructured meshes [20] or Cartesian grid embedded boundary methods [36]. In the former it can be difficult to construct meshes for which a continuous-time random walk approximation of diffusion is well-defined at all mesh voxels when in three dimensions [20]. The latter tends to lose accuracy in voxels cut by the boundary [36]. This may reduce the overall order of accuracy of the resulting spatial discretization that determines the spatial hopping rates in the RDME, thus reducing the accuracy of the RDME in approximating the Brownian motion of molecules, see [36].

For the preceding reasons, in this work we have chosen to focus on developing a convergent numerical method for directly approximating the SDLR model. In particular, our approach does not constrain molecules to remain on a fixed lattice as in the RDME. While our method is presented in one dimension to illustrate that it is converging to the SDLR model, we expect that the method should be well-suited for handling complex geometries in two and three dimensions by treating boundaries as in the Walk on Rectangles algorithm [13]. The latter was designed to generate exact realizations of the Brownian motion of molecules in domains with piecewise linear (planar) boundaries in 2D (3D). The FPKMC can be interpreted as an extension of the Walk on Spheres [45] and Walk on Rectangles [13] methods to systems that involve chemical reactions in simple geometries. We therefore expect it will be straightforward to adapt the FPKMC to handle complex geometries by incorporating the methods of [13].

Exact numerical realizations of the stochastic processes described by the RDME can be generated by the well-known Stochastic Simulation Algorithm (SSA) method [26], which is a Kinetic Monte Carlo (KMC) method [11]. More recently, the First-Passage Kinetic Monte Carlo (FPKMC) method was developed to generate exact realizations of the stochastic processes described by the SDLR model [48, 47, 17, 65]. The method developed in [48, 47, 17] can generate exact realizations of the SDLR model when molecules react instantly upon reaching a fixed separation (a pure-absorption reaction). In [65] this method was modified to generate exact realizations of the SDLR model with a more microscopic partial-absorption reaction mechanism. There molecules (possibly) react based on a specified intrinsic reaction-rate upon collision. This modified version of the FPKMC algorithm was called Green's Function Reaction Dynamics (GFRD) in [65]. In this manuscript we use FPKMC to refer to any of the methods of [48, 47, 17, 65]. (Note, the earlier GFRD method of [69] generates approximations to the stochastic process described by the SDLR model, but differs from that in [65]. The former is not exact, as it assumes the existence of a timestep below which a system of reacting molecules can be decoupled into one and two-body problems, see [69].)

An exact FPKMC method has also been introduced incorporating spatially and temporally varying transition or annihilation rates for single particles [58], which could be used to simulate transitions from diffusive to ballistic modes in models of intracellular transport [41]. The newer GFRD method [65] has been modified to allow for advection due to a *spatially-uniform, constant* velocity field along a one-dimensional track [62]. It should be noted that there are a number of alternative numerical methods, such as Brownian Dynamics, that have also been proposed for approximating the stochastic processes described by the SDLR or Doi models [4, 40, 29]. Each of these methods is approximate, and ultimately based on a discretization in time.

While it is conceptually simple to modify the SDLR model to include drift due to potentials, it is still an open question how best to generate numerical realizations of the underlying stochastic processes described by the model. In this work we propose a dynamic lattice version of the FPKMC method to allow for the inclusion of drift due to a potential. While our Dynamic Lattice FPKMC method (DL-FPKMC) no longer generates exact realizations of the SDLR model, the error introduced in the method is controlled. The method can be extended in a straightforward manner to also include spatially varying diffusion coefficients.

1.2 A DL-FPKMC Method for the SDLR Model with Drift

In this subsection we present an overview introducing the DL-FPKMC method. In the body of the paper, we will develop the details of the method and analyze convergence.

The central idea of the original FPKMC method is to enclose one or two molecules within a ‘protective domain’ that isolates them from all other molecules of the system. A significant change in the state of the system occurs only when a molecule leaves its protective domain or a reaction occurs. In the cases discussed below, first-passage time distributions for such events can be determined from information about the underlying physical system. The first-passage time distributions can then be sampled to determine the time and type of state change that occurs next. This event-driven approach provides an especially efficient simulation algorithm by allowing each update of the algorithm to span the time interval between significant state changes (as opposed to proceeding over many small fixed time steps during which the change in relevant state variables is minor).

In the rather special case of pure Brownian motion in simple domains (spheres or rectangular regions), the first-passage time distributions for a molecule to leave a protective domain [48, 47, 17, 65] or for two molecules to reach a threshold radius for reaction [65] can be computed analytically by solving the diffusion equation. The use of these expressions allows for the generation of exact realizations of the stochastic process described by the SDLR model with the FPKMC. However, for many situations in cell biology, pure Brownian motion does not provide the most realistic description of the movement of molecules as a consequence of active transport, chemical gradients, interactions with cellular structures, etc. In such cases, significant drift terms are inherent to the particle dynamics and can be modeled as arising from a fixed potential field. The DL-FPKMC method we develop extends the FPKMC to allow for such drift. Analytical expressions for the first-passage time distributions from protective domains are no longer possible with the addition of spatially varying drift. In DL-FPKMC, we therefore approximate the drift-diffusion process each molecule undergoes within a protective domain by a continuous-time random walk on a discretized mesh. The ‘hopping rates’ for these walks are determined from the Wang–Peskin–Elston finite-difference discretization of the Fokker–Planck equation [70]. When new protective domains are created during the course of a simulation, they are dynamically meshed. For this reason, our method can be interpreted as a dynamic-lattice master equation model. Unlike the standard RDME, it has the benefit of converging to the SDLR model as the lattice spacing is reduced.

We present results demonstrating both the convergence and accuracy of the DL-FPKMC method in one dimension as the mesh spacing in the discretization is decreased. In particular, we apply our algorithm to the bimolecular reaction $A + B \rightarrow \emptyset$ where the molecules of species A and B undergo drift-diffusion subject to various types of potential functions (smooth, discontinuous, and constant). Our results indicate that the method is approximately second-order accurate for smooth potentials and approximately first-order accurate for discontinuous potentials. In this paper, we focus on convergence of the DL-FPKMC in one dimension because of the availability of exact analytical solutions and high-accuracy numerical solutions with which to assess the error. For a one-dimensional domain containing only one molecule of species A and one molecule of species B , the SDLR model for the reaction system $A + B \rightarrow \emptyset$ can be described by a single two-dimensional PDE for the probability density the particles have not reacted and are located at specified positions. This PDE can be solved numerically to high accuracy with general potential fields using finite difference discretizations, and can be solved analytically when the potential is constant. Having these numerical and analytic solutions allows us to check both the accuracy and the convergence of the DL-FPKMC simulation results. If the domain containing the two molecules were instead two- or three-dimensional, the corresponding PDE would be four- or six-dimensional, respectively, and would therefore be challenging to solve to *high accuracy* by standard PDE discretization techniques. For the two-molecule system in one dimension, we provide detailed numerical results demonstrating the convergence of DL-FPKMC to the SDLR model. For systems with more than two molecules, where high-accuracy solutions to the equations for the probability density of being in a given state are not available, we show more qualitative convergence results.

The FPKMC method was originally presented as an efficient way to simulate reaction-diffusion systems at low particle densities ‘without all the hops’ by using larger ‘superhops’ [48]. While DL-FPKMC uses more hops than FPKMC due to the random walk approximation of molecular motion, we demonstrate that DL-FPKMC maintains efficiency at low particle densities by requiring far fewer hops than fixed lattice methods with comparable resolution. By discretizing each individual protective region, DL-FPKMC allows fine meshes to be used in localized regions when needed for accuracy considerations. Examples where fine meshes may be necessary include resolving bimolecular reactions, boundary conditions, or rapidly varying potential fields. For protective domains in which such features are not present, coarser meshes can be used. In this way the DL-FPKMC offers an alternative to the types of global adaptive mesh methods that have been proposed for RDME-based models [7].

The paper is organized as follows. Section 2 presents our approach for incorporating drift into the SDLR model. In Section 3 we give an overview of the implementation and steps of the FPKMC or DL-FPKMC algorithm to generate realizations of the stochastic process described by the SDLR model. The general discussion in Sections 2 and 3 assumes the molecules move in \mathbb{R}^n . The specific implementation we develop in Section 4 restricts the molecules to intervals in \mathbb{R} , but our technique can be extended to higher dimensions through use of the Walk on Rectangles method [13]. Section 4 presents our numerical method for using a dynamic lattice to incorporate drift into the FPKMC algorithm, and in Section 5 we demonstrate the convergence and accuracy of this DL-FPKMC method. In Section 6 we provide a running time analysis of DL-FPKMC, in which we demonstrate $O(N)$ scaling with the number of molecules in the system and compare DL-FPKMC to a fixed lattice method. Section 7 presents several illustrative applications of DL-FPKMC. In 7.1 we compare the effects of drift due to several potentials on reaction time and location statistics. We conclude in 7.2 by investigating a simplified model of a coupled protein-polymer fiber system, in which two reacting molecules undergo drift-diffusion along a polymer, and may also unbind from the polymer and diffuse in three dimensions. We study the interaction between polymer geometry, binding potentials along the polymer, and unbinding rate.

2 Incorporating Drift into the SDLR Model

In this section a modification of the SDLR model incorporating drift due to a potential is presented. The SDLR reaction-diffusion model, with or without drift, can be described by a system of partial integro-differential equations (PIDEs) for the probability densities of having a given number of molecules of each chemical species at a specified set of positions, similar to the stochastic reaction-diffusion PIDE models in [31] and [15, 16]. Alternatively, one can consider the collection of stochastic processes for the numbers of molecules and positions of each molecule of each chemical species in the system. Due to the high-dimensionality of the system of PIDEs for the probability densities, numerical methods for solving the SDLR model, including FPKMC methods, are typically based on Monte Carlo approaches that approximate the underlying stochastic processes. This section gives the mathematical formulation of the stochastic processes underlying the SDLR reaction-drift-diffusion model. In the remainder of the paper, we develop a Dynamic Lattice First-Passage Kinetic Monte Carlo method (DL-FPKMC) for generating realizations of these stochastic processes. The DL-FPKMC realizations are approximate, but the error is small and goes to zero as the lattice spacing is decreased.

2.1 Drift-Diffusion in the SDLR Model

In the modified SDLR model that includes drift, molecules are modeled as points or hard spheres undergoing drift-diffusion processes. In a system with K chemical species, we label the k^{th} chemical species by S^k , $k = 1, \dots, K$. We denote by $\{M^k(t) : t \geq 0\}$ the stochastic process for the number of molecules of species S^k at time $t \geq 0$. The position vector of the l^{th} molecule of species S^k at time $t \geq 0$ is given by the vector stochastic process $\{Q_l^k(t) : t \geq 0\}$, where $Q_l^k(t) \in \mathbb{R}^n$, $l = 1, \dots, M^k(t)$.

In the absence of any possible chemical reactions we assume the l^{th} molecule of species S^k with position $Q_l^k(t)$ undergoes diffusion with diffusion coefficient D^k and experiences drift due to a potential $V^k(Q_l^k(t))$. In this case, $Q_l^k(t)$ satisfies the stochastic differential equation (SDE)

$$dQ_l^k(t) = \frac{-D^k}{k_B T} \nabla V^k(Q_l^k(t)) dt + \sqrt{2D^k} d\mathbf{W}_l^k(t), \quad (1)$$

where k_B is Boltzmann’s constant, T is absolute temperature, ∇ denotes the gradient in the coordinates of $Q_l^k(t)$, and $\mathbf{W}_l^k(t)$ denotes the standard n -dimensional Wiener process which describes Brownian motion. Note, this equation arises in the over-damped regime in which inertial forces are assumed to be negligible [23]. Our method for generating realizations of this stochastic process will be presented in Section 4. The form of drift due to a potential in Eq. (1) is useful for modeling environmental interactions such as volume exclusion, attractive DNA forces felt by regulatory proteins, and effective potentials felt by molecular motors. It does not allow the possibility of interactions between the diffusing molecules of the chemical system. To incorporate such potentials into our method would be feasible for short-range pair interactions, but for simplicity we assume no potential interactions between molecules.

Table 1: Placement of reaction products.

	<i>One Reaction Product</i>	<i>Two Reaction Products</i>
<i>Unimolecular Reaction</i>	The product is placed at the same location as the reactant.	The products are placed a specified distance apart, with their center of mass at the location of the reactant.
<i>Bimolecular Reaction</i>	The product is placed at the center of mass of the two reactants.	The products are placed a specified distance apart, with their center of mass at the same location as the center of mass of the reactants.

2.2 Reactions in the SDLR Model

When bimolecular and unimolecular reactions are added into the system, the molecules continue to move by the drift-diffusion process in Eq. (1) under the additional constraint that any pair of bimolecular reactants are not allowed to approach closer than their corresponding reaction radius. Upon reaching this reaction radius there are two alternative bimolecular reaction mechanisms that are commonly used in the SDLR model. In a pure absorption reaction the molecules react instantly upon reaching this separation [4], while in a partial absorption reaction the molecules are allowed the additional possibility of having a non-reactive collision [22, 65]. The latter model typically uses an intrinsic reaction rate constant to determine the probability of reaction upon collision (see [22, 37] for possible methods to relate macroscopic and intrinsic bimolecular reaction rates). Mathematically, a pure absorption reaction is modeled through a Dirichlet boundary condition in the corresponding system of PIDEs that describe the SDLR model, while a partial absorption reaction is modeled by a Robin boundary condition [37]. In this work, for simplicity we use the pure absorption mechanism. While this is a more specialized model than the partial absorption reaction, a large number of modeling efforts have made use of the Smoldyn Brownian Dynamics simulator [4], which incorporates the pure absorption reaction mechanism (see [3] for references to these modeling studies). Unimolecular reactions representing internal processes are modeled as occurring with exponentially distributed times based on a specified reaction-rate constant.

We will assume that reaction products are placed at the locations specified in Table 1. In the cases of two reaction products, for either unimolecular or bimolecular reactions, the angular orientation of the product separation vector about the center of mass is chosen randomly, as in [4]. More precise models for where to place the products would require extending the SDLR model to include the individual shapes, sizes, and/or rotational diffusion of molecules.

When using the partial absorption Robin boundary condition-based bimolecular reaction mechanism, the separation distance upon unbinding can be chosen to be exactly the reaction radius. In the case that two products react by the pure absorption Dirichlet boundary condition-based mechanism, such a choice would lead to an immediate re-association reaction. This issue is generally handled through the introduction of an unbinding radius [4]. The unbinding radius is usually calibrated to enforce specified geminate recombination probabilities [4] (i.e. the probability that after unbinding a pair of molecules rebinds instead of diffusing away from each other). In the remainder, we restrict our focus to irreversible bimolecular reactions and assume reactions occur immediately when the separation between two reactants equals a specified reaction radius (a pure-absorption reaction). While we focus on this special case for simplicity, a minor modification of our discretization procedure within protective domains would allow the use of a partial-absorption bimolecular reaction mechanism.

3 First-Passage Kinetic Monte Carlo Methods

This section gives an overview of First-Passage Kinetic Monte Carlo methods, including DL-FPKMC and earlier methods, and then presents the steps for implementing FPKMC or DL-FPKMC.

3.1 Overview of FPKMC Approaches

First-Passage Kinetic Monte Carlo methods have been developed to generate exact realizations of the SDLR model in the absence of drift [48, 47, 17, 65, 58]. These novel algorithms are based on the Walk on Spheres method for solving exit time problems in complicated geometries [45]. They rely on being able to derive exact analytical solutions of the diffusion equation in spheres and rectangular solids. In these FPKMC algorithms, a spherical or rectangular region called a ‘protective domain’ is drawn around every molecule in the system, with the collection of protective domains chosen to be disjoint. The first-passage time for each molecule, meaning the time when the molecule will first hit the boundary of its protective domain, can be sampled exactly using the corresponding analytical solution to the diffusion equation. The molecule that exits its protective domain first is updated to its exit position, and a new protective domain is defined. When two reactants are sufficiently close that a sphere can be drawn that contains only them, the corresponding two-body solution to the SDLR PIDEs can be used to exactly sample a candidate time and location for their reaction [65].

A central feature of each of these prior methods is the assumption that the molecular species undergo purely diffusive stochastic dynamics within their protective domains. When drift due to a potential is present in addition to diffusion, the probability densities for the locations of one or two molecules within their protective domains are no longer described by the diffusion equation, but rather by a Fokker-Planck equation. Let $\Omega \subset \mathbb{R}^n$ denote the overall domain with boundary $\partial\Omega$, and let $U \subset \Omega$ label a protective domain with boundary ∂U . We are interested in the time a molecule first leaves U , leading to a zero Dirichlet boundary condition on ∂U . Let $V(\mathbf{x})$ denote the strength of the potential at $\mathbf{x} \in \Omega$. The probability density, $\rho(\mathbf{x}, t)$, for a single molecule with diffusion coefficient D to be at location \mathbf{x} within its protective domain U at time $t > 0$ evolves according to the equations

$$\begin{aligned} \frac{\partial \rho(\mathbf{x}, t)}{\partial t} &= D \nabla \cdot \left(\rho(\mathbf{x}, t) \frac{\nabla V(\mathbf{x})}{k_B T} + \nabla \rho(\mathbf{x}, t) \right), & \text{on } U, \\ \rho(\mathbf{x}, t) &= 0, & \text{on } \partial U \setminus (\partial U \cap \partial \Omega), \\ \rho(\mathbf{x}, 0) &= \delta(\mathbf{x} - \mathbf{x}_0), \end{aligned} \quad (2)$$

where \mathbf{x}_0 is the initial position of the molecule within the protective domain. If ∂U intersects $\partial \Omega$, the boundary conditions on $\partial U \cap \partial \Omega$ will agree with the boundary conditions on $\partial \Omega$.

For two bimolecular reactants within one protective domain $U \subset \Omega \subset \mathbb{R}^n$, the joint probability density $\rho(\mathbf{x}, \mathbf{y}, t)$ for one molecule to be at location $\mathbf{x} \in U$ and the other molecule to be location $\mathbf{y} \in U$ at time $t > 0$ can be described by a Fokker-Planck equation in \mathbb{R}^{2n} . Define the domain in \mathbb{R}^{2n} to be $W = \{(\mathbf{x}, \mathbf{y}) : \mathbf{x} \in U, \mathbf{y} \in U, \text{ and } \|\mathbf{x} - \mathbf{y}\| > r_R\}$. D_1 and D_2 will denote the respective diffusion coefficients of the two molecules. We define \mathcal{D} to be a $2n \times 2n$ diagonal matrix, with the first n elements of the diagonal equal to D_1 and the next n elements equal to D_2 . Let $V_1(\mathbf{x})$ and $V_2(\mathbf{y})$ be the potential fields that impart drift to the \mathbf{x} molecule and the \mathbf{y} molecule respectively, and define $V(\mathbf{x}, \mathbf{y}) = V_1(\mathbf{x}) + V_2(\mathbf{y})$. The behavior on the boundary ∂W may be different on each of the following three components: the reactive boundary $\partial W_{\text{rxn}} = \partial W \cap \{\|\mathbf{x} - \mathbf{y}\| = r_R\}$, the (possibly empty) intersection with the overall domain boundary $\partial W_{\text{outer}} = (\partial W \cap \{(\mathbf{x}, \mathbf{y}) : \mathbf{x} \in \partial \Omega \text{ or } \mathbf{y} \in \partial \Omega\}) \setminus \partial W_{\text{rxn}}$, and the remaining component $\partial W \setminus (\partial W_{\text{rxn}} \cup \partial W_{\text{outer}})$. Then, $\rho(\mathbf{x}, \mathbf{y}, t)$ satisfies

$$\begin{aligned} \frac{\partial \rho(\mathbf{x}, \mathbf{y}, t)}{\partial t} &= \nabla \cdot \mathcal{D} \left(\rho(\mathbf{x}, \mathbf{y}, t) \frac{\nabla V(\mathbf{x}, \mathbf{y})}{k_B T} + \nabla \rho(\mathbf{x}, \mathbf{y}, t) \right), & \text{on } W, \\ \rho(\mathbf{x}, \mathbf{y}, t) &= 0, & \text{on } \partial W_{\text{rxn}}, \\ \rho(\mathbf{x}, \mathbf{y}, t) &= 0, & \text{on } \partial W \setminus (\partial W_{\text{rxn}} \cup \partial W_{\text{outer}}), \\ \rho(\mathbf{x}, \mathbf{y}, 0) &= \delta(\mathbf{x} - \mathbf{x}_0, \mathbf{y} - \mathbf{y}_0), \end{aligned} \quad (3)$$

where \mathbf{x}_0 and \mathbf{y}_0 are the initial positions of the molecules within the protective domain, and the gradient and divergence operators are in the (\mathbf{x}, \mathbf{y}) coordinates. Similar to the single particle case, if ∂U intersects $\partial \Omega$, the boundary conditions on $\partial W_{\text{outer}}$ will agree with the boundary conditions on $\partial \Omega$. The boundary condition $\rho(\mathbf{x}, \mathbf{y}, t) = 0$ when $\|\mathbf{x} - \mathbf{y}\| = r_R$ models the pure-absorption reaction mechanism. This reactive boundary condition could be modified to use a Robin partial-absorption mechanism if desired. In the remainder we assume all molecules have the same diffusion coefficient and experience the same potential field, so that $D_1 = D_2$ and $V_1 = V_2$. In the case that the potential V is a constant function, Eqs. (2) and (3) reduce to diffusion equations.

Our method for using discretizations of these Fokker-Planck equations to sample times and locations of first-passage and reaction events is described in Section 4.

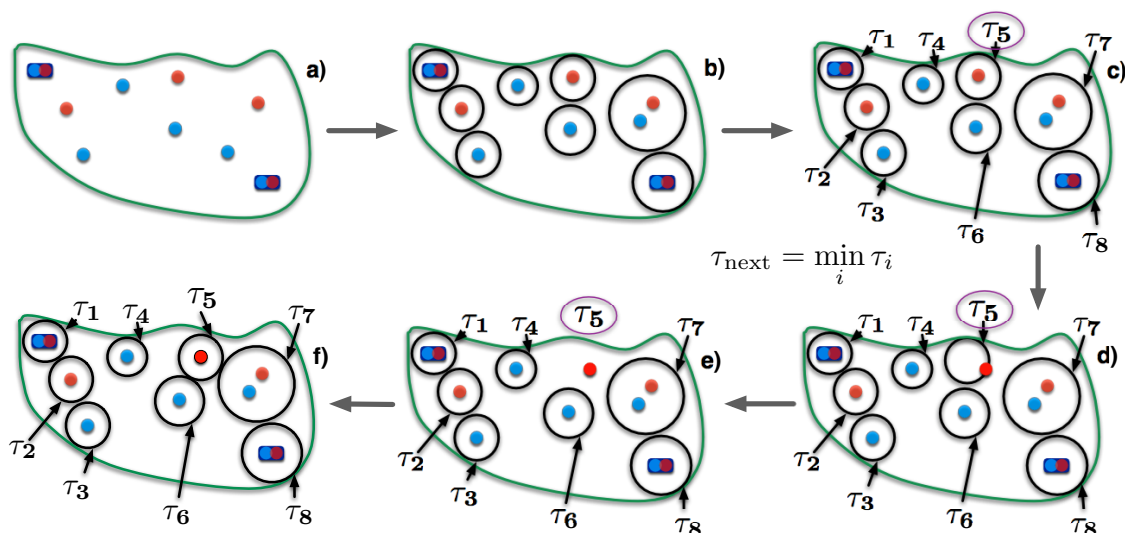


Figure 1: Schematic of the FPKMC or DL-FPKMC algorithm as described in Subsection 3.2. Here, τ_i denotes the next event time for the molecule or pair of molecules in the i^{th} protective domain, and $\tau_{\text{next}} = \tau_5$ is the time of a global event.

3.2 Main Steps of the FPKMC or DL-FPKMC Algorithm

In this subsection we describe the role of protective domains and the processing of events in our implementation of the FPKMC or DL-FPKMC algorithm. We then list the main steps of the algorithm. Our implementation is based on the FPKMC algorithm developed in [48, 47, 17], with some modifications. The content of this section applies to both the FPKMC and DL-FPKMC algorithms. The only theoretical difference between the two methods is the approach for sampling event times within a protective domain. In FPKMC, which can only be used in the case of constant $V(x)$, event times are sampled from *exact* solutions of the diffusion equation. In DL-FPKMC, which allows for arbitrary $V(x)$, event times are *approximated* by generating sample paths of continuous-time random walks on meshes within protective domains (see Section 4).

3.2.1 Protective Domains

To apply the algorithm, every molecule in the system is placed in a protective domain. In one dimension the protective domains are intervals and in higher dimensions the protective domains are usually rectangular or spherical regions. In general, the boundaries of protective domains are absorbing. The boundary of a protective domain can contain a portion of the boundary of the overall spatial domain, in which case the protective domain boundary conditions will depend on the overall domain boundary conditions. We allow protective domains to contain either one or two molecules. Protective domains containing only one molecule are referred to as ‘single protective domains’, and those containing two molecules are referred to as ‘pair protective domains’. Molecules in separate protective domains behave independently. Each molecule undergoes drift-diffusion within its protective domain, and may undergo unimolecular reactions. Two molecules in the same protective domain may additionally participate in bimolecular reactions. To maintain independence when bimolecular reactants are in different protective domains, we require a separation of at least one reaction radius. For non-reacting molecular species we allow for overlap to prevent the size of protective domains from going to zero. Additional details on constructing and updating protective domains are provided in Appendix A.

3.2.2 Events, Times, and Updating

Each event that may occur will have a type, time, and location. The two major event types are first passage from a protective domain and reaction. First passage from a protective domain occurs when a molecule first reaches an absorbing boundary of its protective domain. In DL-FPKMC with general $V(x)$ (resp. FPKMC with constant $V(x)$), times and locations for first-passage events from single protective domains are sampled from probability densities determined from approximate (resp. exact) solutions of Eq. (2). Similarly, for pair protective domains, solutions of

Eq. (3) are used to sample times and locations for first-passage events or for bimolecular reactants to first reach a separation of one reaction radius. The time for a unimolecular reaction to occur is sampled from an exponential distribution with a specified reaction rate, and a corresponding reaction location is sampled from a “no-passage” probability density for the molecule involved (see below).

To facilitate the discussion of these first-passage and reaction events, we use specific names for three times. The ‘global time’ will refer to when the most recent event has occurred, irrespective of its particular type or which molecules were involved. An ‘individual time’ and a ‘next event time’ will be associated with each particular molecule. ‘Individual time’ will refer to when the molecule was last updated, and ‘next event time’ will refer to the sampled time at which the molecule might next undergo an event. Individual times are less than or equal to the global time, and next event times are greater than the global time.

Usually, the individual time and location of a molecule will only be updated when the molecule undergoes a major event (first-passage or reaction). In this case, the time and location of the molecule will be updated to the time and location of the event. However, a molecule can also be updated to any specified time prior to its next event time, by sampling a new position for the molecule within the protective domain from the conditional probability density for the molecule to be at a position within the domain, at the specified time, and not yet have undergone a first-passage or reaction event. This procedure is called a ‘no-passage’ update.

3.2.3 Overall Algorithm

The FPKMC or DL-FPKMC algorithm is carried out according to the following steps:

1. Protective domains are defined around each molecule or pair of molecules, as shown in Figure 1b.
2. The next individual event for each molecule or pair of molecules is determined by sampling an event type, time, and location. In Figure 1c, each next event time is labeled by a τ_i .
3. To determine global events, the individual events are sorted in a priority queue ordered from the shortest event time to the longest event time. For example, τ_5 denotes the shortest event time in Figure 1c.
4. The next global event is determined from the priority queue using the next individual event with the shortest time. The global time and the individual time(s) of the participating molecule(s) are updated to the event time. In the case of a first-passage event for a molecule to leave its protective domain, the molecule’s location is updated to the sampled first-passage location, as shown in Figure 1d. If this molecule is in a pair protective domain with another molecule, the other molecule is no-passage updated to the new global time. In the case of a reaction event, the reaction products are placed at or about the reaction location, as specified in Table 1.
5. Molecules in protective domains that are close to or overlap the newly updated molecules are no-passage updated to the new global time.
6. New protective domains are constructed only for those molecules that have undergone an update to reach the current global time, as shown in Figure 1f. New events are sampled for these updated molecules, and the event times are sorted into the priority queue. All other molecules and events remain unchanged.
7. Steps 4 through 6 are then repeated.

Note that Step 5 is used to keep the sizes of the protective domains from becoming too small [17], in which case the *effective* time steps used in the FPKMC or DL-FPKMC methods could become very short.

We remark that information about the state of any molecule in the system is available for any particular time in the simulation. For instance, if one would like to sample the locations of all molecules at a specified time, this can be obtained by taking the state of the system at the largest global time before or equal to the specified time and then no-passage updating each molecule to the specified time.

3.3 Protective Domain Changes during One Simulation

During simulations, updates are made to the protective domains sequentially as events occur changing the state of the system. To illustrate this process, we consider the simulation in one dimension of the reaction $A + B \rightarrow \emptyset$ starting with one molecule each of A and B and using our DL-FPKMC algorithm. One simulation is shown in Figure 2.

In the left panel of Figure 2, the vertical axis is the number of times that the simulation cycled through Steps 4 to 6 of the algorithm; we call this number N_{update} . In the right panel, the vertical axis is the time of the most recent event. At $N_{\text{update}} = 1$ in this particular run of the simulation, molecule A is first-passage updated to the right endpoint of its initial protective domain. This location is close to the left endpoint of molecule B ’s protective domain, so molecule

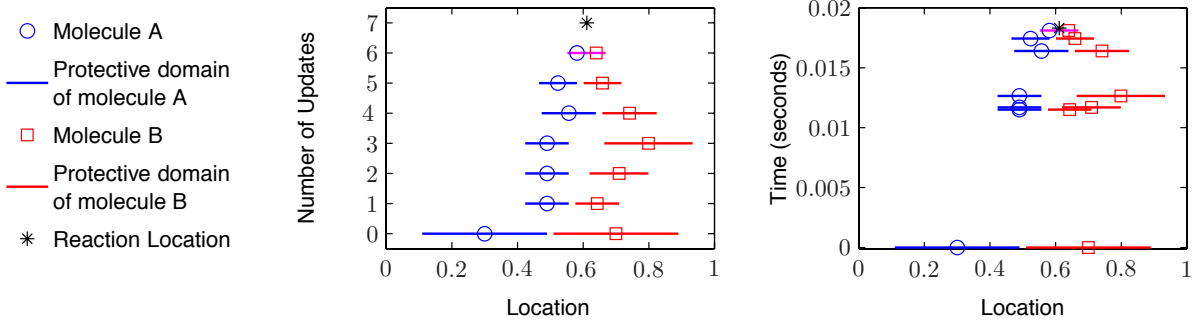


Figure 2: One simulation of the reaction $A + B \rightarrow \emptyset$, with one molecule each of A and B present initially and $V(x) = 0$. Both panels show the same run of the simulation. In the left panel, the vertical axis is the number of times the simulation cycled through Steps 4 to 6 of the algorithm. In the right panel, the vertical axis is the time of the most recent event.

B is no-passage updated and new protective domains are defined around each molecule. From $N_{\text{update}} = 1$ to $N_{\text{update}} = 3$, molecule B is first-passage updated but does not come close to the protective domain of molecule A , so molecule A is not updated. At $N_{\text{update}} = 6$, the distance between molecules A and B is less than a specified pair threshold, so they are placed in a pair protective domain. At $N_{\text{update}} = 7$, the distance between the molecules reaches the reaction radius and the reaction occurs.

4 Propagation of Molecules within Protective Domains in One-Dimensional DL-FPKMC

In this section we introduce a lattice discretization of the Fokker-Planck equation [70] which is used within each protective domain. The discretization is chosen to have the form of a master equation, so that the discretization weights can be interpreted as transition rates for continuous-time random walks by the molecules within each protective domain. In Subsection 4.2 we describe how the Stochastic Simulation Algorithm (SSA) [26, 11] is then used to generate realizations of these random walks within each protective domain, giving the next event times and locations needed by the DL-FPKMC algorithm (see Subsection 3.2.3). It should be stressed that our DL-FPKMC method modifies FPKMC by using this lattice method to propagate molecules *within* their protective domains. To introduce our methods, we consider the case where the simulation domain is a one-dimensional interval (in higher dimensions, the same discretization can be used in each coordinate). We assume that bimolecular reactions occur instantaneously when the reactants' separation reaches the reaction radius. We allow the simulation domain to have reflecting, absorbing, or periodic boundaries. Reflecting boundaries are modeled using zero-flux boundary conditions, and absorbing boundaries are modeled using zero Dirichlet boundary conditions. Protective domains are proper subintervals of the overall domain.

4.1 Lattice Discretization of the Fokker-Planck Equation

In the case of pure diffusion, the probability distributions for first-passage times, first-passage locations, and no-passage locations can all be determined from analytic solutions of the diffusion equation [48, 47, 17, 65]. In contrast, once drift is considered, such analytic approaches are no longer possible in general. Instead one must consider probability densities that satisfy Fokker-Planck equations such as Eqs. (2) and (3), in which we restrict to the case where the drift arises from a spatially varying potential energy function $V(x)$.

To sample event times and locations in DL-FPKMC, we introduce approximations by treating the movement of each molecule within its protective domain as a discrete-space continuous-time Markov chain, more specifically a continuous-time random walk on discrete mesh points. Jump rates between neighboring mesh points are obtained using the Wang–Peskin–Elston [70] (WPE) spatial discretization of the one-dimensional Fokker-Planck equation

$$\frac{\partial \rho(x, t)}{\partial t} = D \frac{\partial}{\partial x} \left(\rho(x, t) \frac{dV(x)}{dx} + \frac{\partial \rho(x, t)}{\partial x} \right). \quad (4)$$

We remark that the factor $(k_B T)^{-1}$ is absorbed into the potential function V . The WPE discretization weights then determine the jump rates (i.e. probabilities per unit time) for molecules to hop from one mesh point to another. In particular, the jump rate for a molecule to hop from the mesh point x_i to a neighboring mesh point x_j , in the case of a uniform mesh of width h , is given by

$$a_{ij} = \begin{cases} \frac{D}{h^2} \frac{V(x_j) - V(x_i)}{\exp[V(x_j) - V(x_i)] - 1} & \text{for } V(x_i) \neq V(x_j) \\ \frac{D}{h^2} & \text{otherwise.} \end{cases} \quad (5)$$

Let $p_i(t)$ be the probability that a molecule is located at mesh point x_i at time t . Then the time evolution of $p_i(t)$ is described by the master equation

$$\frac{dp_i(t)}{dt} = a_{i-1,i} p_{i-1}(t) - (a_{i,i-1} + a_{i,i+1}) p_i(t) + a_{i+1,i} p_{i+1}(t). \quad (6)$$

If $x_{i\pm 1}$ is an absorbing boundary, then $p_{i\pm 1}(t) = 0$ in Eq. (6). We shall extend Eqs. (5) and (6) for non-uniform discretizations in Subsection 4.3 and in Appendix B.

The discretization given by Eq. (5) has the following properties:

- Converges at second-order for smooth potentials, and can handle discontinuous potentials [70].
- Satisfies a discrete version of detailed balance (zero net flux at equilibrium), which helps reduce artificial drift due to numerical discretization errors [70].
- Is consistent with the standard second-order-accurate discretization of the Laplacian operator, in that a_{ij} converges to D/h^2 as $V(x_j) - V(x_i)$ approaches zero.
- *Can be extended to higher dimensions. The jump rates in each coordinate are then given by Eq. (5).*
- Can incorporate a spatially dependent diffusion coefficient $D(x)$. For example, in the case that $D(x)$ is continuous, the constant D in Eq. (5) can be replaced by $[D(x_i) + D(x_j)]/2$ [70].

4.2 Generating Sample Paths

To make use of the WPE discretization, a mesh is defined within each protective domain so that every molecule is located at a mesh point. Rather than numerically solve the master equation (6), and then sample this solution to determine next event times, we generate realizations of the jump process described by Eq. (6). Each molecule then undergoes a continuous-time random walk on the mesh, with the transition rate from a mesh point x_i to a neighboring point x_j given by a_{ij} of Eq. (5). Exact sample paths of the molecules' random walks are generated using the event-driven Stochastic Simulation Algorithm (SSA), specifically Gillespie's "direct method" version of the SSA [26]. In this method, the times of the hops are sampled from exponential distributions. There is no fixed time step. By varying the mesh width, the resolution of this process can be adjusted depending on the desired trade-off between computational efficiency and accuracy. Our specific approach for choosing the mesh width and the locations of mesh points is described in more detail in Subsection 4.4.

Any protective domain endpoints on the interior of the overall domain are absorbing, as are endpoints that coincide with an absorbing boundary of the overall domain. If one endpoint of a protective domain is located at a reflecting boundary of the overall domain that endpoint is made reflecting. Since protective domains are proper subintervals of the overall domain, each protective domain will have at least one endpoint on the interior of the overall domain. Thus, each protective domain either has absorbing Dirichlet boundaries ($\rho = 0$) at both endpoints, or an absorbing boundary at one endpoint and a reflecting zero-flux boundary ($\rho \frac{dV}{dx} + \frac{\partial \rho}{\partial x} = 0$) at the other.

For a newly constructed protective domain containing a single molecule, we determine the molecule's next event time by using the SSA to sample an exact random-walk path for the molecule to hop on the mesh points until it reaches an absorbing boundary of the protective domain. The time that the molecule reaches an absorbing endpoint is the first-passage time, and the endpoint that the molecule reaches is the first-passage location. For pair protective domains with two molecules, we perform random walks for each molecule until either: (i) one molecule reaches an absorbing boundary of the protective domain; or (ii) the distance between the two molecules is equal to the reaction radius r_R . The mesh width for pair protective domains is always chosen to exactly divide r_R , so that the reaction occurs when the two molecules are exactly one reaction radius apart. A no-passage location at any specified time before the next event time can be obtained by finding the last time in the sample path less than or equal to the specified time and taking the location of the molecule at that time.

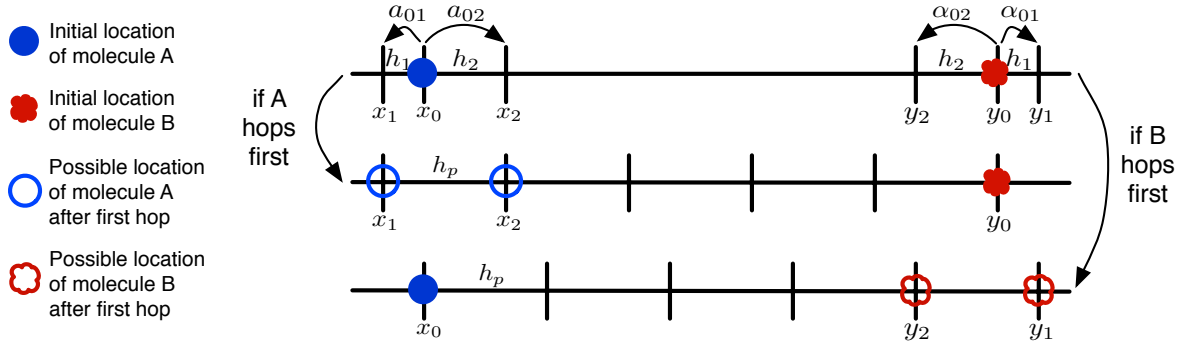


Figure 3: The top row shows the non-uniform sub-meshes that are defined when two molecules are first placed in a pair protective domain. The second (resp. third) row shows the uniform mesh that is chosen if molecule *A* (resp. *B*) hops first. The user-specified uniform mesh width, h_p , is chosen to exactly divide r_R . Let d be the initial distance between the two molecules at the time that the pair protective domain is defined. Then, h_2 is defined to be the remainder of the quotient d/h_p , and $h_1 = h_p - h_2$. By choosing h_1 and h_2 in this way, the distances $|y_0 - x_1|$, $|y_0 - x_2|$, $|y_1 - x_0|$, and $|y_2 - x_0|$ are all exactly divisible by h_p . The rates a_{01} and a_{02} are given by Eq. (7). The SSA is used to simulate a single hop of one of the molecules to a new point on its sub-mesh, after which the new distance between the two molecules will be one of the four distances divisible by h_p listed above. Then, a new mesh of uniform width h_p can be defined so that both molecules lie exactly on mesh points, and the generation of a sample path using the SSA proceeds until one molecule exits the pair protective domain or the distance between the two molecules reaches r_R .

4.3 Discretization for Non-uniform Mesh Cells

Non-uniform mesh cells are used when needed to conform to a boundary or to move molecules onto a uniform mesh where the mesh width exactly divides the reaction radius, as will be described in Subsection 4.4. Let x_0 be the initial location of a molecule on a non-uniform mesh, with x_1 and x_2 denoting the locations of the neighboring mesh points in either direction. Note that we may have either $x_1 < x_0 < x_2$ or $x_2 < x_0 < x_1$ (see Fig. 3, top row). Let $h_1 = |x_0 - x_1|$ and $h_2 = |x_0 - x_2|$. The jump rates from x_0 to x_j for $j = 1, 2$ are given by

$$a_{0j} = \begin{cases} \frac{2D}{h_j(h_1+h_2)} \frac{V(x_j)-V(x_0)}{\exp[V(x_j)-V(x_0)]-1} & \text{for } V(x_i) \neq V(x_j) \\ \frac{2D}{h_j(h_1+h_2)} & \text{otherwise.} \end{cases} \quad (7)$$

The non-uniform discretization in Eq. (7) is derived in Appendix B by modifying the WPE discretization of the Fokker-Planck equation [70]. In the case of constant $V(x)$, the non-uniform discretization (7) reduces to the non-uniform spatial discretization of the Laplacian at a Dirichlet boundary given by equation (20) of [25]. For solving the Poisson equation with Dirichlet boundary conditions, using a uniform interior mesh and non-uniform mesh cells at the boundaries, this discretization is second-order accurate [25]. To our knowledge, Eq. (7) gives a new discretization of the Fokker-Planck equation for non-uniform meshes.

4.4 Choosing the Mesh within Protective Domains

In this subsection we describe how a mesh is defined within each protective domain, given user-specified mesh widths. The convergence tests in Section 5 will demonstrate that DL-FPKMC converges to the underlying SDLR model as the mesh widths are decreased.

Single-molecule protective domains with absorbing boundaries are chosen to be symmetric about the location of the molecule. Let r_{PD} be the distance from the molecule to either endpoint of the protective domain. A maximum mesh width for all single protective domains, h_s^{\max} , is specified by the user. Then, for each individual protective domain, the mesh width h_s is calculated according to the formula

$$h_s = \frac{r_{PD}}{\text{ceil}(r_{PD}/h_s^{\max})}.$$

In this way, h_s is always chosen to be the largest value less than or equal to h_s^{\max} that exactly divides r_{PD} . Generally h_s will satisfy $h_s^{\max}/2 < h_s \leq h_s^{\max}$, unless $r_{PD} \leq h_s^{\max}/2$, in which case $h_s = r_{PD} \leq h_s^{\max}/2$. In practice, h_s

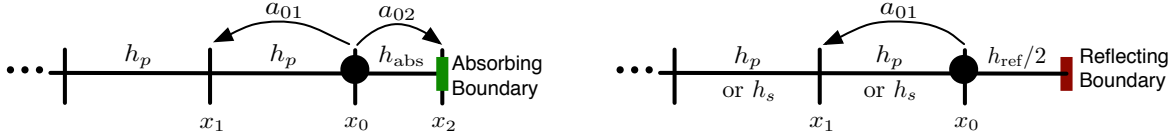


Figure 4: Non-uniform mesh cell at an absorbing Dirichlet boundary of a pair protective domain (left panel), or a reflecting boundary of a pair or single protective domain (right panel). Arrows are shown only where the jump rates differ from those given by Eq. (5) for uniform mesh cells. The point labeled x_0 is the mesh point closest to the boundary (not necessarily the initial location of a molecule when the protective domain is first defined). When using a non-uniform mesh cell at an absorbing boundary, h_{abs} is defined to be the distance from the absorbing boundary to nearest mesh point of the uniform mesh, x_0 . Note that $h_{\text{abs}} \leq h_p$, because otherwise the uniform mesh would have additional mesh points. Then, the jump rates a_{01} and a_{02} in the absorbing boundary case are given by the non-uniform rates in Eq. (7) with $h_1 = h_p$ and $h_2 = h_{\text{abs}}$. At a reflecting boundary, h_{ref} is defined to be twice the distance from the boundary to the nearest mesh point, x_0 . Then, $h_{\text{ref}}/2 \leq h_p$ or h_s . In this case, a molecule cannot jump from x_0 toward the boundary due to the reflecting zero-flux boundary condition. The jump rate a_{01} , going away from the reflecting boundary, is given by Eq. (7) with $h_1 = h_p$ or h_s , and $h_2 = h_{\text{ref}}$.

will almost always be strictly less than h_s^{max} , since it is unlikely that h_s^{max} will exactly divide r_{PD} . After calculating h_s , a uniform mesh with spacing h_s is constructed so that the molecule and both endpoints of the protective domain lie exactly on mesh points. Having the endpoints lie on mesh points allows enforcement of the absorbing Dirichlet boundary conditions at the endpoints without modification of the jumps rates in Eq. (5).

For single-molecule protective domains with one absorbing endpoint and one reflecting endpoint, the mesh width h_s is chosen to be the largest value less than or equal to h_s^{max} that exactly divides the distance from the molecule to the absorbing endpoint. A mesh is defined so that the molecule and the absorbing endpoint lie exactly on mesh points. The mesh is uniform with the exception of one non-uniform cell used immediately adjacent to the reflecting boundary, as shown in Figure 4 (right panel).

In pair protective domains, the mesh width h_p is a user-specified value chosen to exactly divide r_{R} . Each time that two molecules are placed in a new pair protective domain, the initial distance between the molecules will not necessarily be divisible by h_p . Rather than perturbing the molecules, non-uniform mesh cells are used to move one of the molecules, as shown in Figure 3, so that a uniform mesh of width h_p can be defined with both molecules lying exactly on mesh points. Since this uniform mesh is chosen based on the locations of the two molecules, the endpoints of the protective domain may not conform with the mesh. In this case, one non-uniform mesh cell is used at each endpoint, which may be absorbing or reflecting (see Figure 4).

Since h_p is always chosen to exactly divide r_{R} , it necessarily follows that $h_p \leq r_{\text{R}}$. For single molecule protective domains we allow h_s^{max} to be larger than r_{R} . In the convergence studies of the next section, we set $h_s^{\text{max}} = kh_p$ where $k \geq 1$, and hold the ratio of h_s^{max} to h_p constant as both are reduced to study convergence. As discussed above, the actual mesh widths h_s used in single protective domains are almost always strictly less than h_s^{max} , and non-uniform mesh widths are used in both single and pair protective domains. For these reasons, we keep track of the mean of the mesh widths that are actually used in each simulation. In calculating this mean, each mesh width is weighted by the number of times that it is actually used in a sample path. Then, for all simulations performed with fixed h_s^{max} and h_p , we calculate an overall mean mesh width by taking the arithmetic mean of the means for each simulation.

5 Convergence of DL-FPKMC in One Dimension

In this section we perform convergence studies of DL-FPKMC for the annihilation reaction $A + B \rightarrow \emptyset$, where the molecular species A and B undergo drift-diffusion subject to various potentials on the interval $[0, 1]$. Our results demonstrate both the convergence and accuracy of our method as the mesh widths, h_s^{max} and h_p , in the discretization are decreased. We denote by $M^A(t)$ and $M^B(t)$ the number of molecules of A and B , respectively, at time t . In the first set of convergence studies (Subsection 5.1), only two molecules are simulated, $M^A(0) = M^B(0) = 1$. Each simulation runs until the two molecules have reacted. A large number (10^7) of simulations are performed in order to minimize the statistical error, so that the error due to the spatial discretization and the rate of convergence can be studied. In the next set of convergence studies (Subsection 5.2), multiple molecules each of A and B are simulated,

$M^A(0) = M^B(0) = 10$ or $M^A(0) = M^B(0) = 50$, and each simulation runs until all the molecules have reacted. We will denote the i^{th} molecule of species A by A_i , and the location of A_i at time t by $Q_i^A(t)$. B_j and $Q_j^B(t)$ are defined analogously. In the case $M^A(0) = M^B(0) = 1$, we will drop the subscripts i and j .

5.0.1 Potential Functions and Parameters

The convergence studies are performed using three different potential functions: (i) zero potential, $V_{\text{zero}}(x) = 0$ (which results in pure diffusion); (ii) a cosine potential with two energy wells, $V_{\text{cos}}(x) = \cos(4\pi x)$; and (iii) a step potential with one step,

$$V_{\text{step}}(x) = \begin{cases} 2 & \text{if } x < \frac{1}{2} \\ 0 & \text{if } x \geq \frac{1}{2} \end{cases}.$$

The step potential is used to demonstrate that our DL-FPKMC algorithm with the WPE discretization of the Fokker-Planck equation can handle discontinuous potentials. Note that adding a constant to any potential would not change the results, since the Fokker-Planck equation depends on the derivative of the potential but not the potential itself. In particular, any constant potential would produce the same results as $V(x) = 0$.

In all the convergence studies, the length L of the overall domain is 1 unit, the boundaries of the overall domain are reflecting, and the diffusion coefficient D is 1 unit²/sec for both A and B . The values used for the reaction radius r_R will be specified in each subsection. We will use the notation $\mathcal{U}(a, b)$ for the uniform random distribution on the interval (a, b) . The initial locations $Q_i^A(0)$ and $Q_j^B(0)$ are drawn from $\mathcal{U}(a, b)$, where $(a, b) \subseteq (0, L)$ will be specified in each subsection. If $|Q_{i*}^A(0) - Q_{j*}^B(0)| \leq r_R$ for some i^* and j^* , then A_{i*} and B_{j*} will react immediately, at $t = 0$. For $t > 0$, a reaction occurs if $|Q_{i*}^A(t) - Q_{j*}^B(t)| = r_R$.

Note, for most of the convergence studies we run in this section, these initial conditions correspond to non-equilibrium spatial distributions. In the absence of reactions, the equilibrium probability density for a molecule to be at location $x \in (0, L)$ is given by the Gibbs-Boltzmann distribution

$$\frac{e^{-V(x)}}{\int_0^L e^{-V(x)} dx}. \quad (8)$$

For non-constant $V(x)$, the systems with uniformly distributed initial locations on $(0, L)$ are not initially in spatial equilibrium, since the molecule positions are not distributed according to Eq. (8). Furthermore, the systems with initial locations restricted to subintervals of the overall domain are not in spatial equilibrium for any of the potentials used here.

5.0.2 Comparison of DL-FPKMC simulation results in the two-molecule case to analytic and numerical solutions

In general, to describe a stochastic reaction-drift-diffusion system of many molecules by the probability density of having a given number of molecules at specified positions, a large coupled system of partial integro-differential equations is required [31]. In the special case of only two molecules, $M^A(0) = M^B(0) = 1$, with both molecules having the same diffusion coefficient D , the SDLR model for the reaction-drift-diffusion system $A + B \rightarrow \emptyset$ in 1D can be described by a single 2D PDE: a Fokker-Planck equation (or a diffusion equation when V is constant). Let $\rho(x, y, t)$ denote the joint probability density for finding molecule A at location x and molecule B at location y at time $t > 0$. We consider the case where the molecules move in an interval domain of length L with zero-flux boundary conditions at both endpoints. The domain for the corresponding 2D PDE is then $\Omega = \{(x, y) : 0 < x, y < L \text{ and } |x - y| > r_R\}$, and $\rho(x, y, t)$ evolves according to the equations

$$\begin{aligned} \frac{\partial \rho(x, y, t)}{\partial t} &= D \nabla \cdot \left(\rho(x, y, t) \left(\frac{dV(x)}{dx} + \frac{dV(y)}{dy} \right) + \nabla \rho(x, y, t) \right), & \text{on } \Omega, \\ \rho(x, y, t) &= 0, & \text{on } \partial\Omega \cap \{|x - y| = r_R\}, \\ \rho(x, y, t) \frac{\partial}{\partial \boldsymbol{\eta}} (V(x) + V(y)) + \frac{\partial \rho(x, y, t)}{\partial \boldsymbol{\eta}} &= 0, & \text{on } \partial\Omega \setminus \{|x - y| = r_R\}, \end{aligned} \quad (9)$$

where $\boldsymbol{\eta} = \boldsymbol{\eta}(x, y)$ denotes the outward pointing normal at the point (x, y) , and the gradient and divergence operators are in the (x, y) coordinates. The 2D domain for Eq. (9) is illustrated in Appendix C, left panel of Figure 20. When

the initial locations of the two molecules in the DL-FPKMC simulations are drawn from $\mathcal{U}(0, L)$, the corresponding initial condition for the 2D Fokker-Planck or diffusion equation is a constant, $\rho(x, y, 0) = 1/L^2$. Note, in the following we define ρ on $0 \leq x, y \leq L$ by also defining $\rho(x, y, t) = 0$ for $|x - y| < r_R$ and $t > 0$. The 2D Fokker-Planck and diffusion equations (9) can both be solved numerically by finite difference methods, and the diffusion equation can be solved analytically using an eigenfunction expansion. These numerical and analytic solutions are discussed in Appendix C, and provide a baseline against which we compare the results of two-molecule DL-FPKMC simulations in Subsection 5.1.

Let T denote the random variable for the time at which the two molecules react. Using the solution $\rho(x, y, t)$ of Eq. (9), we can calculate the survival probability,

$$S(t) = \Pr [T > t] = \int_0^L \int_0^L \rho(x, y, t) dx dy, \quad (10)$$

and the mean reaction time,

$$\mathbb{E} [T] = - \int_0^\infty t S'(t) dt = \int_0^\infty S(t) dt. \quad (11)$$

Note that $1 - S(t)$ is the reaction time cumulative distribution function (CDF), and $-S'(t)$ is the corresponding density function.

5.0.3 Statistical Error and Discretization Error

In what follows, we will use the term ‘statistical error’ to refer to the difference between the empirical value of a statistic (e.g., mean reaction time) estimated from the DL-FPKMC simulations and the upper, or lower, bound of the 99% confidence interval for the statistic. By ‘discretization error,’ we will mean the difference between the empirical value from the DL-FPKMC simulations and the actual value. In the two-molecule case, actual values are known exactly from the analytic solution $\rho(x, y, t)$ of Eq. (9) when V is constant, and are estimated from the numerical PDE solver described in Appendix C when V is not constant. Note that the measured discretization error is the sum of two unknown quantities: sampling error, and the true discretization error due to the spatially discretized nature of the method.

Since we perform a large number of simulations (10^7) at each mesh width in the two-molecule case, the statistical error is quite small, generally between 0.04% and 0.19% for reaction time statistics. Although we perform fewer simulations (4×10^4) when using multiple molecules each of species A and B, the statistical error is still reasonably small, generally between 0.4% and 1%. Our results show that as the mesh width is decreased, the discretization error rapidly decreases to below the statistical error. This demonstrates that the DL-FPKMC algorithm converges and accurately resolves the underlying reaction-drift-diffusion processes.

5.1 Two-Molecule Convergence Studies

In this subsection we consider the reaction $A + B \rightarrow \emptyset$ for a system with $M^A(0) = M^B(0) = 1$. Here, the initial locations $Q^A(0)$ and $Q^B(0)$ are drawn randomly from $\mathcal{U}(0, 1)$; the reaction radius r_R is 0.02 units; and the pair threshold r_{pair} is equal to $2r_R$ (i.e. the molecules are placed in a pair protective domain when $|Q^A(t) - Q^B(t)| \leq r_{\text{pair}}$). We study the convergence of several statistics as the mesh widths h_s^{max} and h_p are reduced.

For $V = 0$, the errors in the DL-FPKMC simulation results are generally calculated relative to the exact analytic solution, as determined from the eigenfunction expansion in Appendix C. For V_{cos} and V_{step} , the errors are relative to the numerical solution from the PDE solver described in Appendix C. In the PDE solver, we use either the Crank–Nicolson method or the Twizel–Gumel–Arigu method for the time-stepping as explained in the appendix.

As the mesh widths in the DL-FPKMC simulations are decreased, the empirical values of the statistics studied approach the actual values for all three potentials. In each of Figures 5, 6, and 8–10, the first panel will show results for $V = 0$, the second panel for V_{cos} , and the third panel for V_{step} .

5.1.1 Mean Reaction Times

Let $\mathbb{E}_{\text{emp}}[T]$ be the empirical mean reaction time calculated from the DL-FPKMC simulations. Define $\mathbb{E}_{\text{upp}}[T]$ and $\mathbb{E}_{\text{low}}[T]$ to be, respectively, the upper and lower bounds of the 99% confidence interval for the empirical mean reaction time. We denote by $\mathbb{E}_{\text{act}}[T]$ the exact analytic mean reaction time in the case that $V = 0$, or the mean

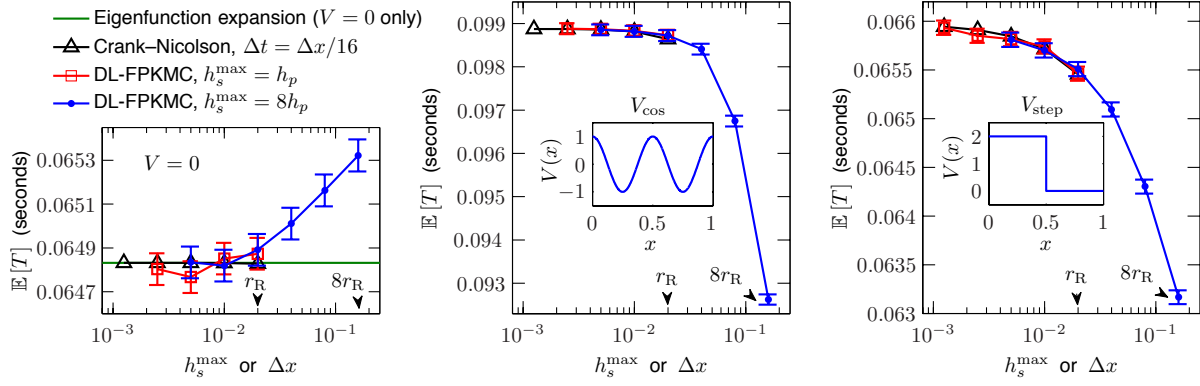


Figure 5: Convergence of mean reaction time, $\mathbb{E}[T]$, for the two-molecule $A + B \rightarrow \emptyset$ reaction, as the mesh width is decreased. Note the expanded scales of the vertical axes. Each DL-FPKMC data point shows $\mathbb{E}_{\text{emp}}[T]$ from 10^7 simulations, with 99% confidence intervals. The resulting values of $\mathbb{E}[T]$ from solving Eq. (9) using our Crank–Nicolson numerical PDE solver are shown here in the $V = 0$ case to demonstrate the solver’s accuracy (see Appendix C for more detail). The mean reaction time calculated from the numerical PDE solution was resolved to an absolute error tolerance of less than 10^{-5} for V_{\cos} and less than 10^{-4} for V_{step} . The PDE solver error tolerances are smaller than the DL-FPKMC statistical errors, allowing the PDE solver estimate for $\mathbb{E}[T]$, determined with the finest value of Δx , to be used in the absence of an analytic value when V is non-constant.

reaction time determined from the numerical PDE solution in the $V \neq 0$ cases (see Eqs. (11) and (27)). We calculate the relative error by

$$\frac{|\mathbb{E}_{\text{act}}[T] - \mathbb{E}_{\text{emp}}[T]|}{\mathbb{E}_{\text{act}}[T]} \pm \frac{|\mathbb{E}_{\text{bd}}[T] - \mathbb{E}_{\text{emp}}[T]|}{\mathbb{E}_{\text{act}}[T]} \quad \text{where } \mathbb{E}_{\text{bd}}[T] = \mathbb{E}_{\text{upp}}[T] \text{ or } \mathbb{E}_{\text{low}}[T]. \quad (12)$$

The 99% confidence interval for $\mathbb{E}_{\text{emp}}[T]$ is symmetric about the mean, so $\mathbb{E}_{\text{upp}}[T] - \mathbb{E}_{\text{emp}}[T] = \mathbb{E}_{\text{emp}}[T] - \mathbb{E}_{\text{low}}[T]$. If $\mathbb{E}_{\text{act}}[T]$ is contained in the interval $(\mathbb{E}_{\text{low}}[T], \mathbb{E}_{\text{upp}}[T])$, then the discretization error $|\mathbb{E}_{\text{act}}[T] - \mathbb{E}_{\text{emp}}[T]|$ is less than the statistical error $|\mathbb{E}_{\text{bd}}[T] - \mathbb{E}_{\text{emp}}[T]|$.

Figure 5 shows $\mathbb{E}_{\text{emp}}[T]$ plotted against h_s^{max} as the mesh widths are varied, and in Figure 6 the relative errors in $\mathbb{E}_{\text{emp}}[T]$ calculated by Eq. (12) are plotted against the mean mesh width. The insets in Figure 5 show the respective potentials. As the mesh widths are reduced, the discretization errors decrease to less than the corresponding statistical errors. Note that the statistical errors are very small since 10^7 simulations were performed at each mesh width.

We estimate the rate of convergence to be approximately second-order for V_{\cos} and approximately first-order for V_{step} . This is consistent with the convergence rates of the WPE discretization of the Fokker–Planck equation for smooth and discontinuous potentials. In the $V = 0$ case, it is difficult to draw a conclusion about the rate of convergence since the discretization errors are small relative to the statistical errors; however, for the same reason, we can conclude that the results are very accurate in this case.

5.1.2 Survival Probabilities

For each mesh width, the empirical survival probability $S_{\text{emp}}(t)$ and the associated 99% confidence bounds are calculated using the MATLAB function ‘ecdf’. The confidence bounds determined by ‘ecdf’ are symmetric to within numerical precision at all but a few points, which are at the tails of the distributions. $S_{\text{act}}(t)$ will denote the analytic survival probability for $V = 0$, and the numerical survival probability determined from the PDE solver for $V \neq 0$ (see Eqs. (10), (26) and Appendix C for more information). Figure 7 plots the empirical survival probabilities $S_{\text{emp}}(t)$ with 99% confidence bounds, and shows convergence of $S_{\text{emp}}(t)$ to $S_{\text{act}}(t)$ as the mesh widths are reduced.

To quantify the magnitude of the error, we calculate the distances between $S_{\text{emp}}(t)$ and $S_{\text{act}}(t)$ using the following methods. The discrete L^1 , L^2 , and L^∞ norms of a function $u(t)$ are given by

$$\|u(t)\|_{L^1} = \sum_i |u(t_i)| \Delta t_i, \quad \|u(t)\|_{L^2} = \left\{ \sum_i u(t_i)^2 \Delta t_i \right\}^{\frac{1}{2}}, \quad \|u(t)\|_{L^\infty} = \max_i |u(t_i)|. \quad (13)$$

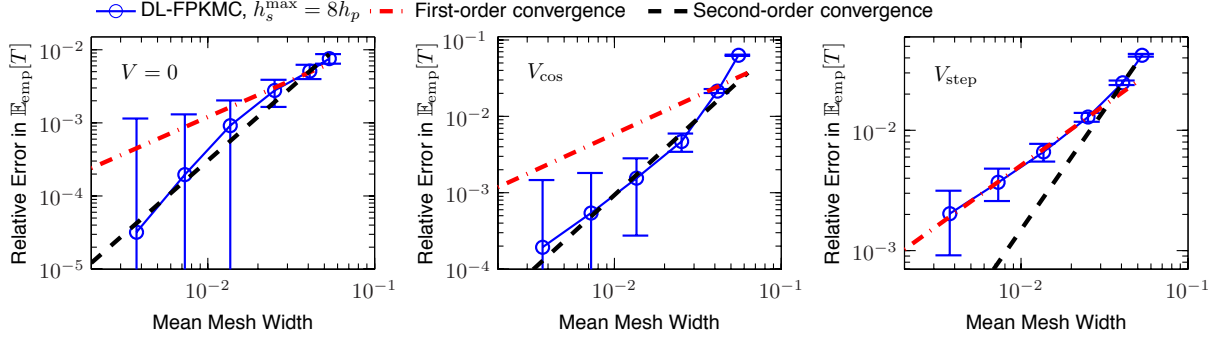


Figure 6: Relative errors (12) in the empirical mean reaction time, $\mathbb{E}_{\text{emp}}[T]$, for the two-molecule $A + B \rightarrow \emptyset$ reaction. In the $V = 0$ case, the errors in $\mathbb{E}_{\text{emp}}[T]$ from the DL-FPKMC simulations are calculated relative to the exact analytic $\mathbb{E}_{\text{act}}[T]$ given by Eq. (27). For $V \neq 0$, the errors in $\mathbb{E}_{\text{emp}}[T]$ are calculated relative to the $\mathbb{E}_{\text{act}}[T]$ determined from the numerical solution of Eq. (9) using the Crank–Nicolson method with the finest value of Δx (see Appendix C). Note that the vertical axes have different scales in each panel. Here $h_s^{\text{max}} = 8h_p$, and the ratio is held constant as both are decreased by successive halving. Each data point is based on 10^7 simulations with fixed values of h_s^{max} and h_p . The error bars are determined by Eq. (12) using the 99% confidence intervals for the empirical mean reaction times. Note, the error bars are symmetric (and similar in size for the different mesh widths), but appear asymmetric (and larger for finer meshes) due to the log scale. Relative errors are not plotted for the simulations with $h_s^{\text{max}} = h_p \leq r_R$, because the discretization errors are small compared to the statistical errors (cf. Fig. 5, red lines with square markers).

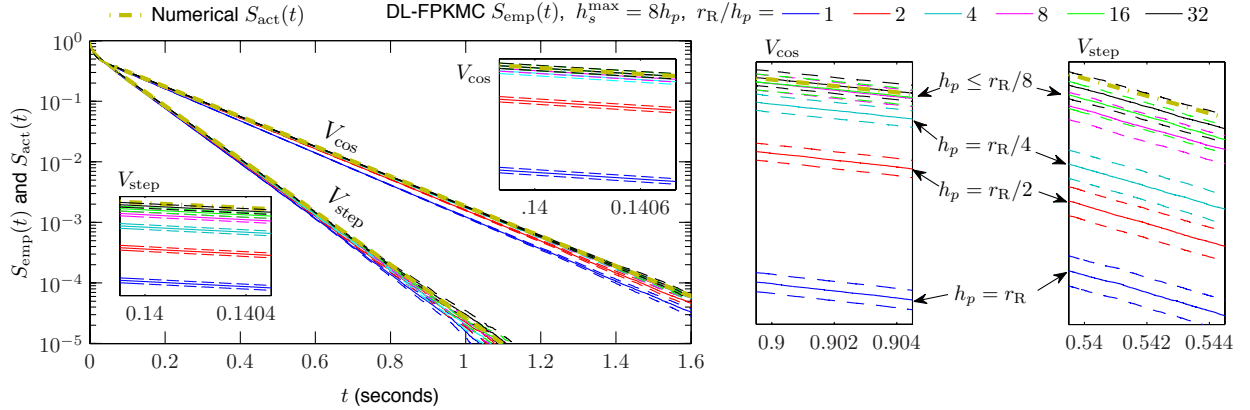


Figure 7: Convergence of empirical survival probabilities, $S_{\text{emp}}(t)$, for the two-molecule $A + B \rightarrow \emptyset$ reaction with V_{cos} and V_{step} . Each empirical survival probability function is based on 10^7 simulations. The dashed lines show 99% confidence bounds. (Note that $r_R = 0.02$ units is constant; r_R/h_p changes as h_p and h_s^{max} are successively halved.) $S_{\text{emp}}(t)$ from the $V = 0$ case is not plotted because it is difficult to visually distinguish between the results for different mesh widths. In the case $V = 0$ and $h_p = r_R/32$, the analytic $S_{\text{act}}(t)$ is contained within the 99% confidence bounds of $S_{\text{emp}}(t)$ at every time point t_i at which $S_{\text{act}}(t)$ was evaluated ($> 6 \times 10^4$ time points); for $h_p = r_R/8$ and $h_p = r_R/16$, $S_{\text{act}}(t)$ is contained within the confidence bounds of $S_{\text{emp}}(t)$ at more than 96% of the time points. This demonstrates that the discretization error is small compared to the statistical error.

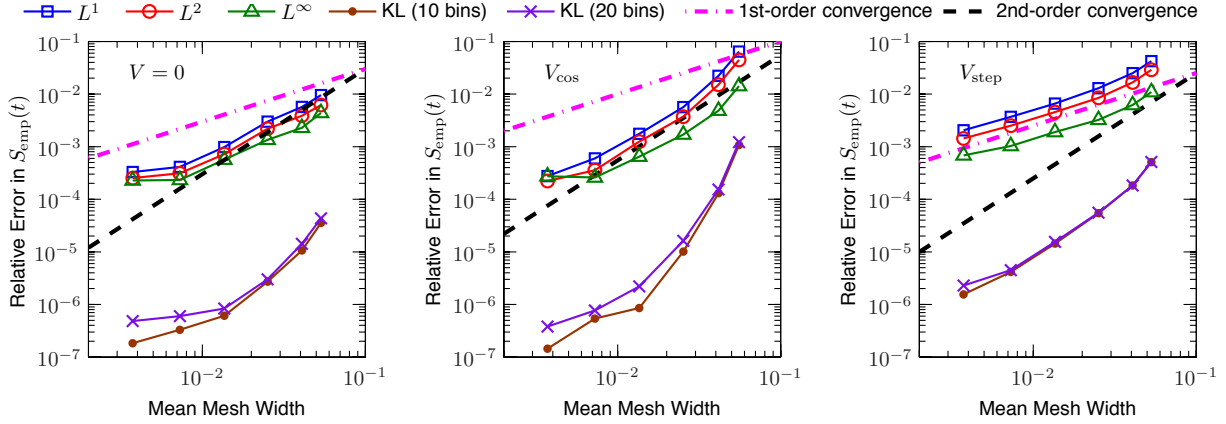


Figure 8: Errors in the empirical survival probability $S_{\text{emp}}(t)$, relative to $S_{\text{act}}(t)$, for the two-molecule $A + B \rightarrow \emptyset$ reaction: relative errors measured in norm (14) and KL divergence (16). Here $h_s^{\text{max}} = 8h_p$ as both are decreased. Each empirical survival probability function is based on 10^7 simulations. Note that the slight plateauing of the errors for finer meshes is due to sampling error, as illustrated in Fig. 7 by the size of the confidence bounds relative to the smaller distance between $S_{\text{emp}}(t)$ and $S_{\text{act}}(t)$.

The relative error for $S_{\text{emp}}(t)$ we report in each norm is then given by

$$\frac{\|S_{\text{act}}(t) - S_{\text{emp}}(t)\|}{\|S_{\text{act}}(t)\|}, \quad (14)$$

where the norms are evaluated on the interval $t \in [0, S^{-1}(10^{-6})]$ with $\Delta t_i = t_{i+1} - t_i$. The time points, t_i , used in evaluating the norms correspond to those at which the numerical PDE solutions were calculated (see Appendix C for more information). In the $V = 0$ case, the analytic expression for the survival probability was evaluated at those same t_i 's. In all cases, the empirical DL-FPKMC survival probabilities were linearly interpolated to obtain values at every t_i .

The L^∞ error is equivalent to the Kolmogorov distance between distributions [12], which is a statistical distance. Another statistical distance is the Kullback–Leibler (KL) divergence [39], which is a measure of the information lost when a distribution $G(t)$ is used to approximate a (true) distribution $F(t)$. For continuous probability distributions, let $g(t)$ and $f(t)$ be the corresponding densities. Then, the KL divergence of $G(t)$ from $F(t)$ is given by

$$KL(F||G) = \int f(t) \ln \left(\frac{f(t)}{g(t)} \right) dt. \quad (15)$$

For discrete distributions

$$KL(F||G) = \sum_i F_i \ln \left(\frac{F_i}{G_i} \right). \quad (16)$$

Since empirical densities obtained from Monte Carlo simulations are noisy, we approximate $KL(S_{\text{act}}||S_{\text{emp}})$ of Eq. (15) by binning the data into a finite number of time intervals and then applying Eq. (16). We use either 10 or 20 bins: 9 or 19 evenly-sized bins on the interval $t \in [0, S^{-1}(0.01)]$, and one bin for $t > S^{-1}(0.01)$. This approximation of the KL divergence becomes noisier as more bins are used. Note, while the KL divergence can be interpreted as a measure of the difference between two distributions, it does not define metric.

Figure 8 shows the relative errors measured in norm (14) and the KL divergence (16), plotted against the mean mesh width. The magnitude of the relative errors and the estimated convergence rates for $S_{\text{emp}}(t)$ are similar to those for $\mathbb{E}_{\text{emp}}[T]$. For each measure we see that the error in the survival probabilities decreases as the mesh widths are reduced. For finer mesh sizes, the discretization error becomes small compared to the statistical error (see Fig. 7). As such, the observed rate of convergence decreases and the graphs become less regular in Fig. 8.

5.1.3 Discrete Joint Spatial Probabilities

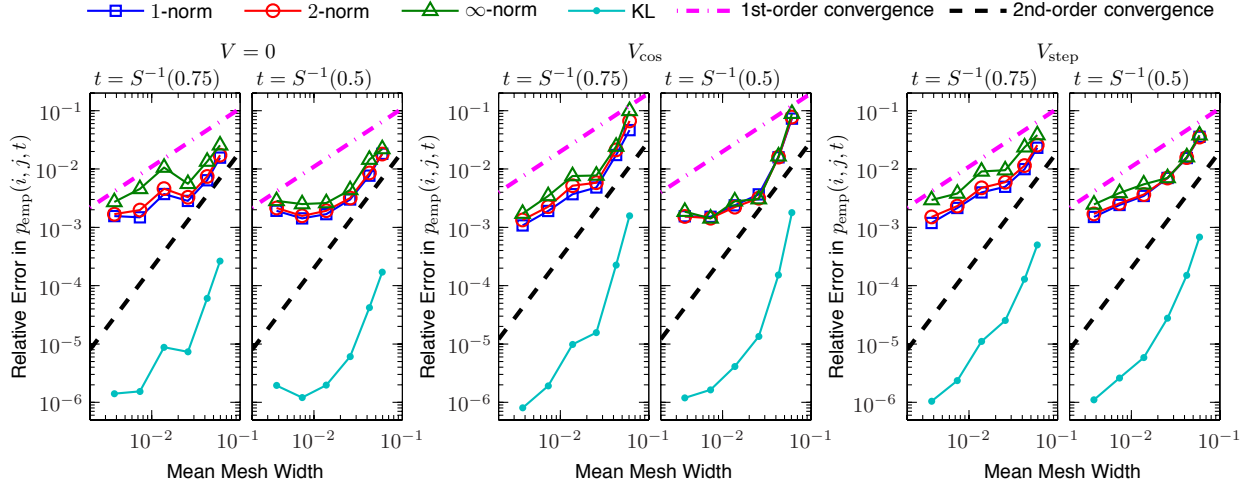


Figure 9: Errors in the empirical joint spatial probabilities $p_{\text{emp}}(i, j, t)$ at $t = S_{\text{act}}^{-1}(0.75)$ and $t = S_{\text{act}}^{-1}(0.5)$ for the two-molecule $A + B \rightarrow \emptyset$ reaction. For all graphs we divide the domain into 25 equally-sized bins ($1 \leq i, j \leq 5$). The errors are calculated relative to $p_{\text{act}}(i, j, t)$, as determined from the PDE solver with Twizell–Gumel–Arigu time-stepping described in Appendix C. Here $h_s^{\text{max}} = 8h_p$ as both are decreased. Each data point is based on 10^7 simulations. At $t = S_{\text{act}}^{-1}(0.75)$ (resp. $t = S_{\text{act}}^{-1}(0.5)$) the two molecules have not yet reacted in approximately 75% (resp. 50%) of the simulations. We also recorded $p_{\text{emp}}(i, j, t)$ at $t = S_{\text{act}}^{-1}(0.25)$, however the convergence results were more strongly affected by noise, since the molecules had already reacted by that time in most of the simulations.

Recall that the joint density, $\rho(x, y, t)$, is the solution of Eq. (9). We now study the convergence of the joint probability that $(Q^A(t), Q^B(t))$ is contained in one of $N_x \times N_x$ subregions of the domain Ω of Eq. (9). For $1 \leq i, j \leq N_x$, define the discrete joint probability function for the locations of the two molecules at time t by

$$\begin{aligned} p_{\text{act}}(i, j, t) &= \Pr \left[\frac{i-1}{N_x} L < Q^A(t) < \frac{i}{N_x} L, \frac{j-1}{N_x} L < Q^B(t) < \frac{j}{N_x} L \right] \\ &= \int_{(j-1)L/N_x}^{jL/N_x} \int_{(i-1)L/N_x}^{iL/N_x} \rho(x, y, t) dx dy. \end{aligned} \quad (17)$$

We study the convergence of the empirical $p_{\text{emp}}(i, j, t)$ from the DL-FPKMC simulations at two fixed times, $t = S_{\text{act}}^{-1}(0.75)$ and $t = S_{\text{act}}^{-1}(0.5)$, where $p_{\text{emp}}(i, j, t)$ is determined by binning the locations of the molecules at time t into the $N_x \times N_x$ subregions.

We calculate the relative error in $p_{\text{emp}}(i, j, t)$ at a fixed time t by

$$\frac{\|p_{\text{act}}(i, j, t) - p_{\text{emp}}(i, j, t)\|}{\|p_{\text{act}}(i, j, t)\|}, \quad (18)$$

where the norms in the numerator and denominator are given by

$$\begin{aligned} \|q(i, j, t)\|_1 &= \sum_{i=1}^{N_x} \sum_{j=1}^{N_x} |q(i, j, t)|, \quad \|q(i, j, t)\|_2 = \left\{ \sum_{i=1}^{N_x} \sum_{j=1}^{N_x} q(i, j, t)^2 \right\}^{\frac{1}{2}}, \\ \text{or } \|q(i, j, t)\|_\infty &= \max_{1 \leq i \leq N_x} \max_{1 \leq j \leq N_x} |q(i, j, t)|, \end{aligned} \quad (19)$$

with $q = p_{\text{act}} - p_{\text{emp}}$ for the numerator and $q = p_{\text{act}}$ for the denominator.

We also calculate the KL divergence (16) of $p_{\text{emp}}(i, j, t)$ from $p_{\text{act}}(i, j, t)$. Since the KL divergence is only defined for probabilities that sum to one, we include an extra “bin” representing that probability that the two molecules have already reacted, which is given by $1 - S(t) = 1 - \sum_{i=1}^{N_x} \sum_{j=1}^{N_x} p(i, j, t)$. The relative errors and KL divergence are shown in Fig. 9. We see similar convergence behavior as in the previous subsection, with the errors clearly decreasing for coarser mesh widths, but plateauing as sampling error becomes dominant at smaller mesh widths.

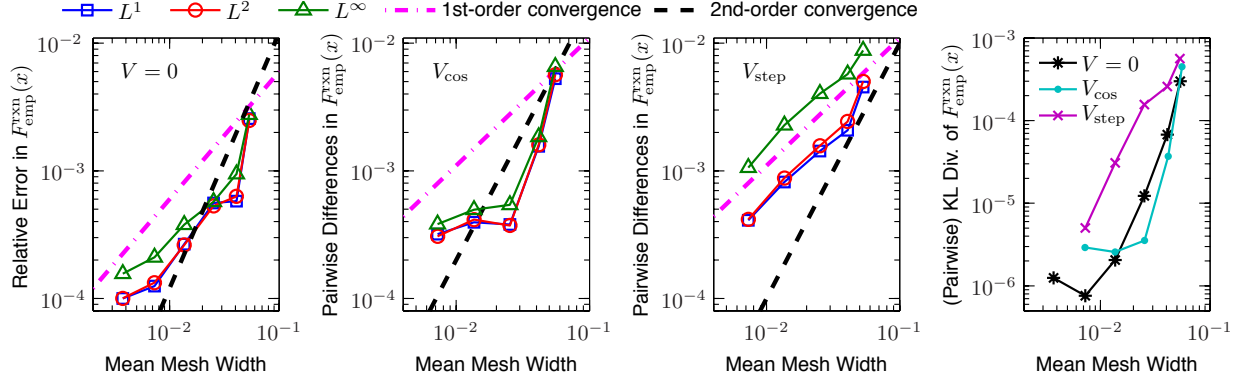


Figure 10: Errors in $F_{\text{emp}}^{\text{rxn}}(x)$, the empirical reaction location CDF, for the two-molecule $A + B \rightarrow \emptyset$ reaction: errors relative to the analytic $F_{\text{act}}^{\text{rxn}}(x)$ for $V = 0$, and pairwise relative differences between $F_{\text{emp}}^{\text{rxn}}(x)$ from successive mesh widths for V_{cos} and V_{step} . The pairwise relative differences are plotted against the mean mesh width for the coarser of the two meshes. Here $h_s^{\text{max}} = 8h_p$ as both are decreased. Each empirical CDF is based on the simulations in which the two molecules react after time $t = 0$, out of 10^7 total simulations. The plateaus in the errors or differences at the finer mesh widths are due to sampling error. For example, in the case of V_{cos} , the 99% confidence bounds for $F_{\text{emp}}^{\text{rxn}}(x)$ from the two finest mesh widths overlap at more than 96% of the 10^4 points at which they were evaluated.

5.1.4 Reaction Location Distributions

For a reaction between A and B , the location of the reaction will be taken to be $Q^{\text{rxn}} = (Q^A(t) + Q^B(t))/2$ where t is the time of the reaction. Then $F^{\text{rxn}}(x) = \Pr[Q^{\text{rxn}} \leq x]$ is the cumulative distribution function for the reaction locations. In studying convergence of the empirical $F_{\text{emp}}^{\text{rxn}}(x)$ as the mesh widths are reduced, we consider only those reactions that occur after $t = 0$. (When $|Q^A(0) - Q^B(0)| \leq r_R$, the reaction occurs immediately at $t = 0$ regardless of the mesh width.) For the parameters used here approximately 3.96% of the reactions occur at $t = 0$.

For $V = 0$, the exact distribution $F_{\text{act}}^{\text{rxn}}(x)$ can be calculated analytically from the solution of Eq. (9). See Eq. (28) of Appendix C for the analytic result. In this case, we study convergence by comparing $F_{\text{emp}}^{\text{rxn}}(x)$ from the DL-FPKMC simulations to the analytic $F_{\text{act}}^{\text{rxn}}(x)$. For the $V \neq 0$ cases, we examine the successive pairwise differences between $F_{\text{emp}}^{\text{rxn}}(x)$ from the DL-FPKMC simulations as the mesh widths are decreased. In all cases, the distributions $F^{\text{rxn}}(x)$ are evaluated at 10^4 evenly spaced points.

For $V = 0$, the relative errors in each norm (13) are calculated by $\|F_{\text{act}}^{\text{rxn}}(x) - F_{\text{emp}}^{\text{rxn}}(x)\| / \|F_{\text{act}}^{\text{rxn}}(x)\|$. For V_{cos} and V_{step} , the pairwise relative differences are calculated by the preceding formula with $F_{\text{emp}}^{\text{rxn}}(x)$ from the finer of the two meshes replacing $F_{\text{act}}^{\text{rxn}}(x)$. The corresponding density is approximated by binning the reaction locations into 20 evenly-sized bins, so that the KL divergence (16) can be calculated (comparing to the analytic values for $V = 0$, and comparing the empirical values from successive mesh widths for V_{cos} and V_{step}). The results are shown in Fig. 10. Note that the relative errors and pairwise relative differences are all less than 1%. Although the results for the spatial statistics are more affected by noise (Figs. 9, 10), the convergence rates appear similar to those for the time statistics (cf. Figs. 6, 8).

5.2 Results of Multiple-Molecule Convergence Studies

In the convergence studies for multiple molecules undergoing the reaction $A + B \rightarrow \emptyset$, we start the simulations with either 20 molecules ($M^A(0) = M^B(0) = 10$) or 100 molecules ($M^A(0) = M^B(0) = 50$). In the 20-molecule simulations: $r_R = 0.02$ units; $r_{\text{pair}} = 2r_R$; $Q_i^A(0) \sim \mathcal{U}(0.1, 0.4)$ and $Q_j^B(0) \sim \mathcal{U}(0.6, 0.9)$ for $1 \leq i, j \leq 10$. In the 100-molecule simulations: $r_R = 0.001$ units; $r_{\text{pair}} = 4r_R$; $Q_i^A(0)$ and $Q_j^B(0) \sim \mathcal{U}(0, 1)$ for $1 \leq i, j \leq 50$. Two molecules A_{i*} and B_{j*} are placed in a pair protective domain if they are closer to each other than to any other molecules of the opposite type, i.e. if

$$|Q_{i*}^A(t) - Q_{j*}^B(t)| = \min_i |Q_i^A(t) - Q_{j*}^B(t)| = \min_j |Q_{i*}^A(t) - Q_j^B(t)|,$$

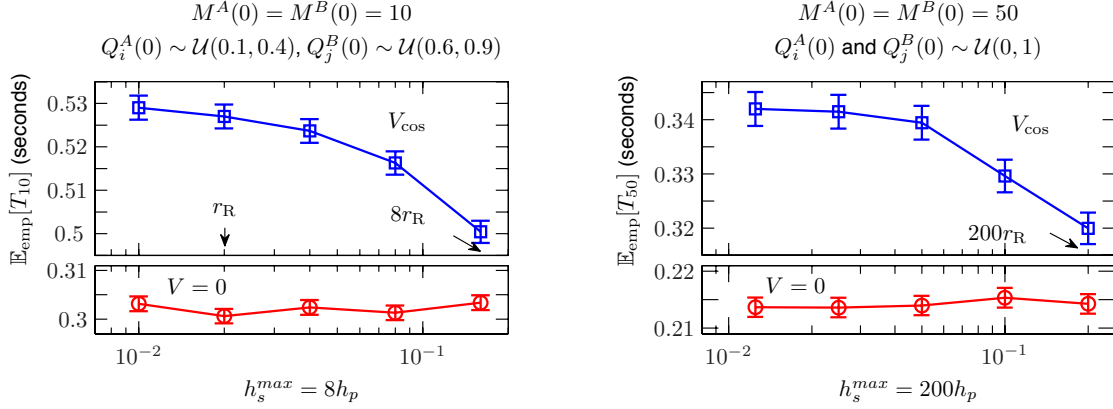


Figure 11: Mean time for all molecules to react via the reaction $A + B \rightarrow \emptyset$. Error bars show 99% confidence intervals, based on 4×10^4 simulations per data point. *Left panel:* $r_R = 0.02$ units. *Right panel:* $r_R = 0.001$ units.

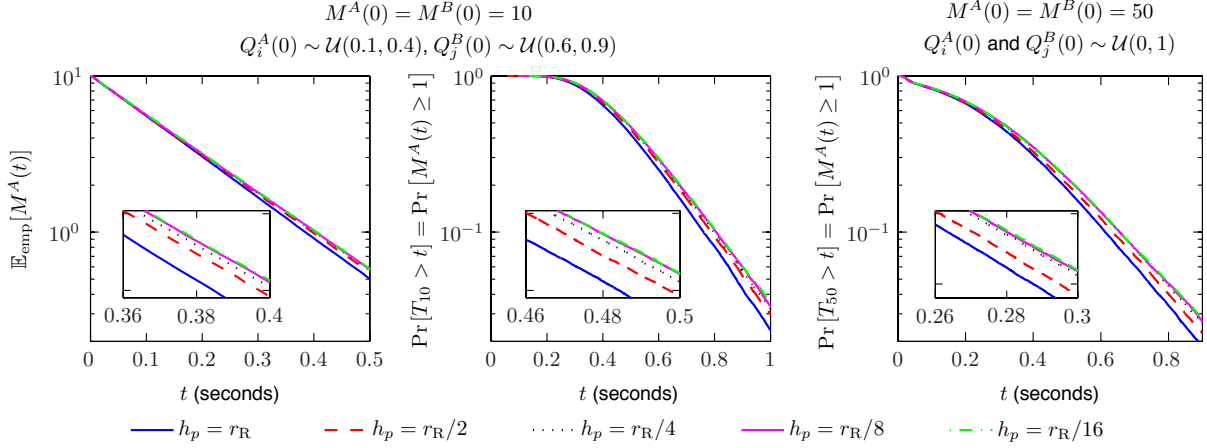


Figure 12: Mean number of molecules of A remaining at time t , $\mathbb{E}_{\text{emp}}[M^A(t)]$ (left panel), and probability that at least one molecule of A remains at time t , $\Pr[M^A(t) \geq 1]$ (center and right panels). $V = \cos(4\pi x)$. Each graph is based on 4×10^4 simulations. $\mathbb{E}_{\text{emp}}[M^A(t)]$ is not plotted in the case $M^A(0) = M^B(0) = 50$, because the results for the different mesh widths are essentially indistinguishable until $\mathbb{E}_{\text{emp}}[M^A(t)] \lesssim 4$. *Left and center:* $r_R = 0.02$ units, $h_s^{\max} = 8h_p$. *Right:* $r_R = 0.001$ units, $h_s^{\max} = 200h_p$.

and if the distance between them satisfies

$$|Q_{i*}^A(t) - Q_{j*}^B(t)| \leq r_{\text{pair}}$$

and

$$|Q_{i*}^A(t) - Q_{j*}^B(t)| \leq r_R + \min(\min_{i \neq i*} |Q_{i*}^A(t) - Q_i^A(t)|, \min_{j \neq j*} |Q_{j*}^B(t) - Q_j^B(t)|). \quad (20)$$

The last condition in Eq. (20) was added to prevent the length of the protective domain of a molecule, say A_i , from approaching zero when A_i is close to another molecule of the same type, say A_{i*} , where A_{i*} would otherwise have been placed in a pair with B_{j*} .

Each simulation runs until all of the molecules have reacted. Let T_n denote the random variable for the time at which the n^{th} reaction occurs. Since we are working with the irreversible reaction $A + B \rightarrow \emptyset$, we have that $M^A(t) = M^A(0) - n$ for $t \in [T_n, T_{n+1})$, and similarly for $M^B(t)$. Figure 11 shows the empirical mean time for all molecules to react; this is $\mathbb{E}_{\text{emp}}[T_{10}]$ when $M^A(0) = M^B(0) = 10$ and $\mathbb{E}_{\text{emp}}[T_{50}]$ when $M^A(0) = M^B(0) = 50$. With these values of $M^A(0)$ and $M^B(0)$, the SDLR model described in Section 2 will correspond to a large coupled system of partial integro-differential equations for the probability densities of having a specified number of molecules

at specified locations. It is no longer feasible to solve these equations numerically to obtain high-accuracy solutions for assessing the empirical convergence of our DL-FPKMC method. As such, we now estimate the accuracy of reaction time statistics by comparing DL-FPKMC results at coarser mesh widths to results obtained with the finest mesh width.

When $V(x) = \cos(4\pi x)$ (Fig. 11, top panels), we see convergence as the mesh width is decreased. The percent difference between $\mathbb{E}_{\text{emp}}[T_{10}]$ for the coarsest mesh width compared to the finest mesh width is approximately 5.4%; this percent difference for $\mathbb{E}_{\text{emp}}[T_{50}]$ is approximately 7%. These differences are comparable in size to the explicitly calculated discretization error of approximately 6.4% at the coarsest mesh width for $\mathbb{E}_{\text{emp}}[T]$ in the two-molecule case (previous subsection).

When $V = 0$ (Fig. 11, bottom panels), the confidence intervals for all mesh widths overlap, indicating that the discretization error is less than the statistical error even for the coarsest mesh width. The statistical errors when $V = 0$ are between 0.49% and 0.81%. If the unknown discretization error here is comparable in size to the known discretization error in $\mathbb{E}_{\text{emp}}[T]$ in the two-molecule case, which was approximately 0.87% at the coarsest mesh width, that would provide an explanation for why we can not observe convergence when $V = 0$.

$\mathbb{E}_{\text{emp}}[M^A(t)]$ is the mean number of A molecules remaining at time t , and $\Pr[M^A(t) \geq 1]$ is the probability that at least one molecule of A remains at time t . Figure 12 shows convergence of $\mathbb{E}_{\text{emp}}[M^A(t)]$ and $\Pr[M^A(t) \geq 1]$ as the mesh width is decreased, in the case $V(x) = \cos(4\pi x)$. Results are not plotted for the $V = 0$ case, because the confidence bounds for different mesh widths overlap; this indicates that the results are resolved to within the statistical error, even for coarser mesh widths.

6 Running Time Analysis

In this section we demonstrate that the running time of the DL-FPKMC algorithm when simulating the $A + B \rightarrow \emptyset$ reaction scales linearly with the number of molecules in the system. We also compare the computational performance of DL-FPKMC to a second method in which all molecules hop on a fixed, global, uniform lattice. Both methods were implemented in MATLAB, and an attempt was made to take advantage of reasonable and standard optimizations. That said, we make no claim that our implementation of either method provides optimal computational performance. All DL-FPKMC and fixed lattice simulations were performed in MATLAB on a Sun Fire X4600 M2 x64 server. The server was configured with four AMD Opteron Model 8220 processors (2.8 GHz dual-core) and 16 GB of RAM.

In both methods, bimolecular reactions occur when the distance between two reactants is exactly equal to r_R . To enforce this condition in the fixed lattice method, the lattice spacing h will be chosen to equal r_R . We set $V(x) = 0$, so the spatial hopping rates in the fixed lattice method are simply D/h^2 . The results of the convergence studies in Section 5 indicate that in DL-FPKMC taking $h_p \approx r_R$ and $h_s^{\max} \approx L/50$ is sufficient to resolve the reaction and diffusion processes to within statistical error for $n \leq 10^7$ simulations. For biologically relevant parameter values, e.g. $L = 10\mu\text{m}$ and $r_R = 1\text{nm}$, this will allow h_s^{\max} in DL-FPKMC to be a couple orders of magnitude larger than h in the fixed lattice method without compromising accuracy.¹

To our knowledge, the only reaction system that has previously been simulated *in one dimension* using any FPKMC-type method is the $A + A \rightarrow \emptyset$ [48, 47] reaction, in which any two molecules annihilate as soon as they collide. In contrast, for the reaction system $A + B \rightarrow \emptyset$, molecules of the same type do not react. As mentioned in Subsection 3.2, we allow the protective domains of non-reacting molecules to overlap to prevent the size of protective domains from going to zero when two non-reacting molecules approach each other. We expect that this issue could also be addressed by allowing protective domains to contain more than two molecules. In order to simulate the same underlying process with both DL-FPKMC and the fixed lattice method, non-reacting molecules in the fixed lattice simulations are allowed to occupy the same lattice site and cross each other.

6.1 Parameters

In comparing the DL-FPKMC and fixed lattice methods, the following parameters values are used: $L = 10\mu\text{m}$, $r_R = 1\text{nm}$, $D = 10\mu\text{m}^2/\text{sec}$, and $V(x) = 0$. The overall simulation domain, the interval $(0, L)$, has reflecting boundaries. The initial number of molecules of A and B are equal, $M^A(0) = M^B(0)$, and each simulation runs until

¹Since $V(x) = 0$, in the fixed lattice method each possible spatial hop is equally likely. This allows optimization of the underlying Stochastic Simulation Algorithm [26, 11]. Incorporating drift into the fixed lattice method would give spatially-varying hopping rates, so additional computational cost might be required to sample which molecule hops and in which direction.

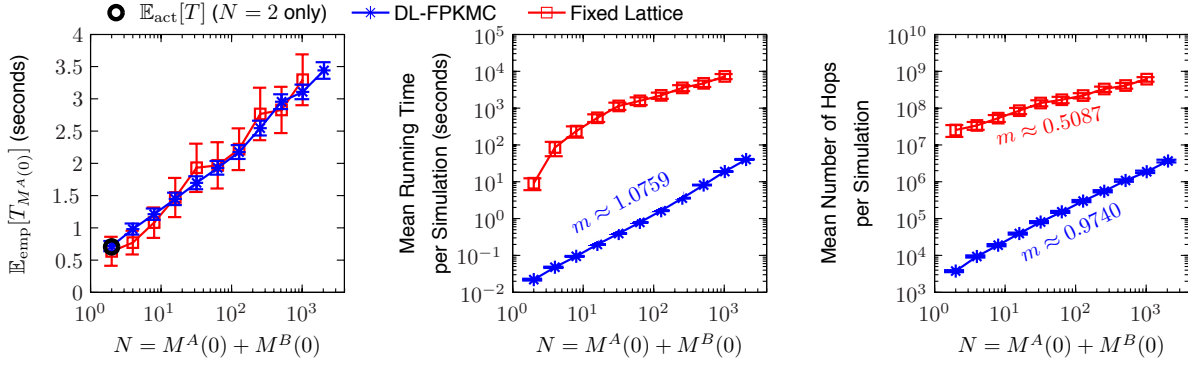


Figure 13: Comparison of DL-FPKMC and fixed lattice methods for the reaction $A + B \rightarrow \emptyset$ as the number of molecules present initially, $N = M^A(0) + M^B(0)$, is increased. $M^A(0) = M^B(0)$, $Q_i^A(0)$ and $Q_j^B(0) \sim \mathcal{U}(0, L)$ for $1 \leq i, j \leq M^A(0)$, $L = 10\mu\text{m}$, $r_R = 1\text{nm}$, $D = 10\mu\text{m}^2/\text{sec}$, and $V(x) = 0$. Each DL-FPKMC data point is based on 10^3 simulations, and each fixed lattice data point is based on 10^2 simulations. Error bars indicate 99% confidence intervals.

all molecules have reacted. The initial locations of molecules are uniformly distributed over the interval $(0, L)$. In both DL-FPKMC and the fixed lattice method, if the initial distance between a molecule of A and a molecule of B is less than or equal to r_R , then they react immediately. All later reactions occur when the distance between an A molecule and a B molecule equals r_R . In the fixed lattice simulations, $h = r_R = 1\text{nm}$. In DL-FPKMC, $h_s^{\max} = L/50 = 200\text{nm}$, $h_p = r_R = 1\text{nm}$, and $r_{\text{pair}} = 50\text{nm}$. To check that using a coarser value for h_s^{\max} than h_p is still sufficient to obtain accurate results, we ran 10^6 simulations with $M^A(0) = M^B(0) = 1$. In this case the exact mean reaction time, $\mathbb{E}_{\text{act}}[T]$, is known analytically, see Eq. (27). Using the preceding parameters, the resulting $\mathbb{E}_{\text{emp}}[T]$ from the DL-FPKMC simulations agrees with $\mathbb{E}_{\text{act}}[T]$ to within statistical error, which is approximately 0.34%.

6.2 Results of Running Time Analysis

Figure 13 compares the simulation results and computational performance of DL-FPKMC to those of the fixed lattice method as the total number of molecules in the system, $N = M^A(0) + M^B(0)$, is varied. As shown in the left panel, the resulting values of $\mathbb{E}_{\text{emp}}[T_{M^A(0)}]$, the mean time for all molecules to react within the simulations, from the two methods agree to within statistical error. The running time (center panel) for DL-FPKMC is two to three orders of magnitude faster than the running time for the fixed lattice. DL-FPKMC also requires fewer hops than the fixed lattice by two to three orders of magnitude (right panel). The slope of the line for DL-FPKMC on the log-log plot of running time (center panel) indicates that the method is approximately $O(N)$, i.e., the running time scales linearly with the number of molecules, $N = M^A(0) + M^B(0)$. Although the fixed lattice method has better scaling with N , it would not appear to become more efficient than DL-FPKMC until N is substantially larger than 10^5 . At that large a number of molecules, it is common to transition to more macroscopic stochastic reaction-diffusion models.

As the number of molecules in the system is increased, the proportion of running time spent on different steps of the DL-FPKMC algorithm changes. For the parameter values used in this section, the changes in proportions of running time as N is increased from 2 to 2048 are as follows (approximated using the MATLAB ‘profile’ function):

- Generating sample paths: decreases from 67% to 38%,
- Identifying neighboring molecules and defining new protective domains for updated molecules based on locations of neighbors: increases from 17% to 52%,
- Determining which molecules (possibly none) to no-passage update after each first-passage update: decreases from 4% to 3%,
- Sorting the event queue: decreases from 7% to 3%.

These percentages could vary substantially for different parameter values and mesh widths, but we expect the overall trends would hold.

As was described in Subsection 4.2, the DL-FPKMC algorithm generates a sample path for each molecule within its protective domain until a first-passage or reaction event occurs. Whenever a molecule is no-passage updated before its next event time, part of its sample path goes unused. The mean number of hops per simulation shown in

Figure 13 (right panel) is based on the total number of hops in all sample paths that are generated, not just the hops that are actually used. Particularly long paths tend to be generated for protective domains touching an overall domain boundary, since molecules can only exit through one endpoint of such protective domains. If we cap the length of single-molecule protective domains that are near the boundaries, then the total number of hops decreases, but the number of times that the protective domains are updated increases and the overall running time also increases. Some guidelines for and difficulties in optimizing the partitioning of space among protective domains in FPKMC are discussed in [17], but we have not yet attempted to address this difficult optimization problem.

6.3 Expectations for Future Studies

It is expected that the implementation of DL-FPKMC in higher dimensions can be done in such a way as to maintain the $O(N)$ scaling for the following reasons:

- FPKMC in two and three dimensions can be implemented to have $O(N)$ scaling [17]. One might expect identifying neighboring molecules to be more costly in higher dimensions, however, in practice the near-neighbor list (NNL) method allows for constant per event costs, leading to $O(N)$ scaling for the overall method [17];
- The only algorithmic difference between DL-FPKMC and FPKMC is that DL-FPKMC generates sample paths within protective domains using continuous-time random walks, whereas FPKMC samples from analytic solutions of the diffusion equation;
- Since the fraction of running time spent generating sample paths in DL-FPKMC decreases as N increases, the scaling of overall running time as N increases is expected to depend mainly on other steps of the algorithm. These steps can all be implemented in the same way in DL-FPKMC as in FPKMC.

See Table 5 of [14] for the computational cost of several reaction-diffusion methods, including methods for simulating the SDLR model and the RDME. The original, approximate GFRD [69] and Smoldyn [4] exhibit $O(N)$ scaling with the total number of molecules for diffusive movements and $O(\sum_{N_R} \prod_{S \in R} N_S)$ scaling for reactive distances, where N_R is the number of reaction channels and N_S is the number of molecules of a given species [14]. We expect FPKMC and DL-FPKMC will have similar scaling with number of reaction channels.

Although $O(N)$ scaling would eventually cause the computational cost to become too high for very large N , many systems of biological interest could still be simulated at low cost. FPKMC has been used to simulate systems with 10^8 particles in one dimension [48] and 216×10^6 particles in three dimensions [47]. For many relevant biological systems, the number of molecules would be less than 1000, or even in the single digits in many cases. For example, the chemotaxis system in bacteria shows “sensitivity to concentrations as low as 3 ligands per cell volume” [63]. In mammalian cells, the number of molecules of a particular mRNA was on the order of tens or hundreds of molecules per cell [52]. Ref. [8] measured the copy numbers of approximately 7300 proteins in a common human tissue culture cell line (U2OS), and found that proteins involved in signaling, cell communication, regulation of cellular processes, catalysis of post-translational modifications, and lipid metabolism tend to be present at copy numbers of less than 500 per cell.

7 Applications

In Subsection 7.1 we investigate the effects of drift due to several potentials on reaction time and location statistics. In Subsection 7.2 we present a simplified model of a protein-polymer system, in which two reacting molecules undergo drift-diffusion along a polymer, and may also unbind from the polymer and diffuse in three dimensions. We study the interaction between polymer geometry, binding potentials along the polymer, and unbinding rates.

7.1 Comparison of Potentials

To demonstrate the contrasting effects that can be produced by different drifts, we consider the reaction $A + B \rightarrow \emptyset$ where the molecules diffuse within various potential energy landscapes. We consider the following three cases: (i) zero potential, $V(x) = 0$; (ii) a one-well potential, $V(x) = \cos(2\pi x)$; and (iii) a two-well potential, $V(x) = \cos(4\pi x)$. We use a domain of length $L = 1$ unit with reflecting boundaries, and diffusion coefficient $D = 1$ unit²/sec for both molecular species A and B .

In the absence of reactions, the equilibrium probability density for a molecule to be at location $x \in (0, L)$ is given by the Gibbs-Boltzmann distribution in Eq. (8). We compare the Gibbs-Boltzmann distributions for each of the three

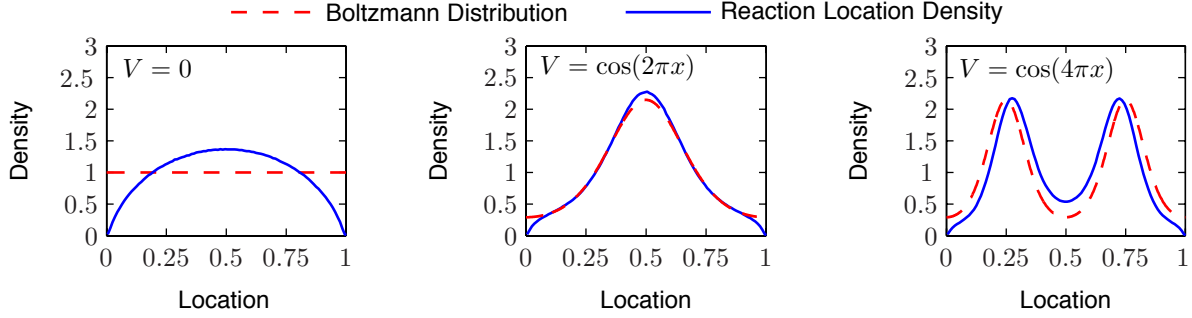


Figure 14: Reaction locations from $A + B \rightarrow \emptyset$ DL-FPKMC simulations with $M^A(0) = M^B(0) = 1$, and the Gibbs-Boltzmann distribution for each potential. The reaction location is $(Q^A(t) + Q^B(t))/2$, where t is the time of the reaction. Each graph of reaction locations is based on 10^7 simulations. $r_R = 0.02$. $h_s^{\max} = h_p = r_R/8$. $Q^A(0)$ and $Q^B(0) \sim \mathcal{U}(0, 1)$. The plotted densities were determined by binning the reaction locations into 100 bins.

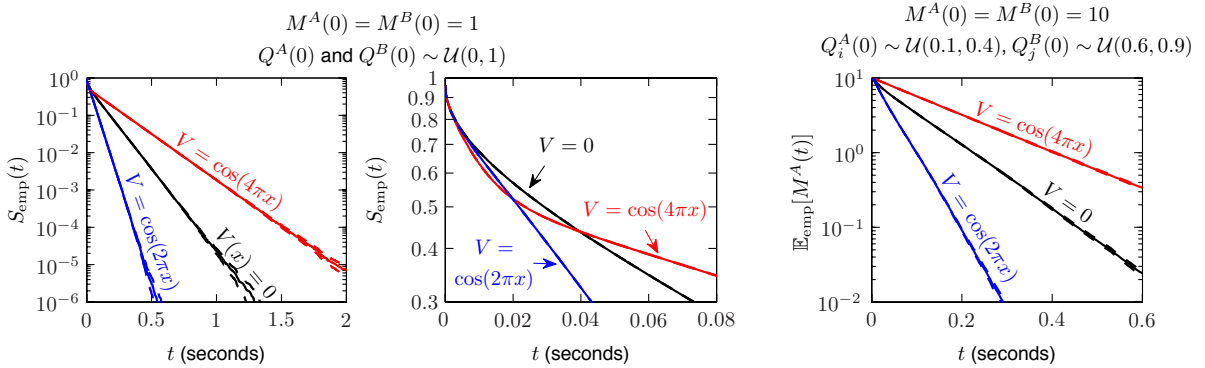


Figure 15: *Left and center panels:* Empirical survival probability $S_{\text{emp}}(t)$ for the two-molecule $A + B \rightarrow \emptyset$ reaction. Both panels show the same survival probabilities, however the axes have different scales. The dashed lines show 99% confidence bounds based on 10^7 simulations. $r_R = 0.02$. $h_s^{\max} = h_p = r_R/8$. *Right panel:* Empirical mean number of molecules of A remaining at time t , for the reaction $A + B \rightarrow \emptyset$ with $M^A(0) = M^B(0) = 10$. The dashed lines show 99% confidence bounds based on 4×10^4 simulations. $r_R = 0.02$. $h_p = r_R/16$. $h_s^{\max} = 8h_p$.

potentials to the reaction locations from the $A + B \rightarrow \emptyset$ DL-FPKMC simulations in the particular case of two molecules, $M^A(0) = M^B(0) = 1$. The results are shown in Figure 14. The potentials serve to spatially “confine” molecules, in the sense that molecules are most likely to be found in locations where the potential energy is lowest. Consequently, the reactions are most likely to occur in such low energy locations.

As would be expected, the mean reaction time for the two-molecule $A + B \rightarrow \emptyset$ reaction is faster with the one-well potential (~ 0.03481 sec) than with no potential (~ 0.06483 sec), while slower with the two-well potential (~ 0.09887 sec). Figure 15 (left and center panels) compares the survival probabilities $S_{\text{emp}}(t)$ for the three different potentials. The semi-log graphs of $S_{\text{emp}}(t)$ for all three potentials appear linear except at short times, indicating that the reaction time distributions could be described by exponential distributions for larger times (Fig. 15, left panel). For $V = 0$, this is as to be expected since the survival probability distribution is known analytically and is given by the eigenfunction expansion (26) in Appendix C. At short times (Fig. 15, center panel), the graphs of $S_{\text{emp}}(t)$ for the different potentials are not linear and behave differently from each other. Initially, reactions occur more quickly with the two-well potential than with either the one-well potential or no potential. However, after $S_{\text{emp}}(t)$ has decreased to about 50%, reactions occur more slowly with the two-well potential than with the other potentials. As would be expected, if the initial locations of the two molecules are in the same well of a potential, then they tend to react more quickly; whereas, if the two molecules start in different energy wells, then the time until they react tends to be longer.

Figure 15 (right panel) shows $\mathbb{E}_{\text{emp}}[M^A(t)]$, the mean number of molecules of A remaining at time t , when $M^A(0) = M^B(0) = 10$, $Q_i^A(0) \sim \mathcal{U}(0.1, 0.4)$ and $Q_j^B(0) \sim \mathcal{U}(0.6, 0.9)$. In this case, $\mathbb{E}_{\text{emp}}[M^A(t)]$ could be described by exponential distributions for all three potentials. In the case of $M^A(0) = M^B(0) = 50$ with $Q_i^A(0)$ and

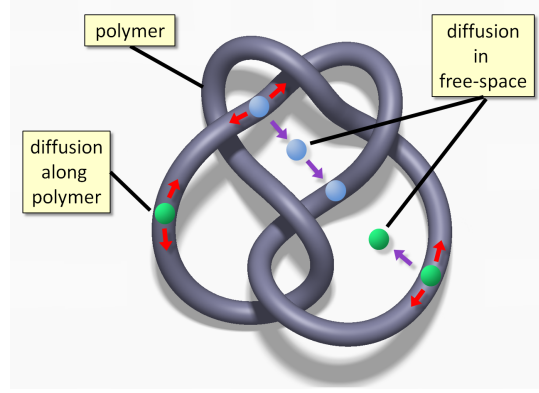


Figure 16: Biopolymer diffusion-excursion search and protein-protein interactions. The geometry of an individual biopolymer or network is expected to be influential in the search kinetics of proteins which diffuse in one dimension along the biopolymers, but may also detach to undergo excursions in three dimensions.

$Q_j^B(0) \sim \mathcal{U}(0, 1)$, $\mathbb{E}_{\text{emp}}[M^A(t)]$ is not plotted but behaves very similarly to $S_{\text{emp}}(t)$ in the two-molecule case with $Q^A(0)$ and $Q^B(0) \sim \mathcal{U}(0, 1)$ (Fig. 15, left and center panels).

7.2 Role of Biopolymer Geometry and Binding Potentials in Protein Diffusive Search

Many proteins diffuse effectively in one dimension by adhering loosely to biopolymer filaments, such as actin, microtubules, or DNA [2]. In the case of DNA regulatory proteins, single molecule experiments and theoretical work indicate that observed rapid kinetic rates are achieved by a search process involving a combination of one-dimensional diffusion of the protein sliding along the DNA in conjunction with three-dimensional diffusive excursions [71, 56, 59, 27, 60, 44, 30, 9]. The geometry of the individual biopolymer or network of biopolymers is expected to play an influential role in such search kinetics. We introduce a model to investigate this phenomena in the diffusion of proteins that interact with biopolymers having basic knotted closed-loop configurations, see Figure 16. In our model we also allow for position-dependent forces acting on the proteins, such as might occur from heterogeneities in DNA sequence or protein binding sites. We perform simulations of two proteins undergoing a search process until they encounter each other on a biopolymer. The process involves one-dimensional drift-diffusion along the polymer in combination with absorption/desorption events associated with excursions from the polymer. For example, this process could model the formation of a regulatory complex at a non-specific DNA binding site. Movement along the polymer is simulated using the drift-diffusion DL-FPKMC method introduced in the preceding sections. The effects of the biopolymer geometry are taken into account through the absorption/desorption statistics computed by numerically solving a diffusion equation in three dimensions for each specified biopolymer configuration. We remark that the model and methods we introduce are readily extended to more complex geometries, polymer networks, and filament bundles.

7.2.1 Model of the Biopolymer Drift-Diffusion Process and Three-Dimensional Excursions

The biopolymer is represented geometrically as a one-dimensional filament embedded within a three-dimensional space Ω . The heterogeneity along the biopolymer strand, for example changes in DNA sequence, density of bound proteins, or other chemical factors, are taken into account through the potential in the drift-diffusion process. To account for diffusive excursions in three dimensions, we introduce desorption and absorption events for the protein from the biopolymer. Let λ_{off} be the first-order rate at which a protein desorbs from the biopolymer. We assume the protein must undergo a conformational change before regaining affinity to bind to the biopolymer (otherwise it would instantly re-absorb at the desorption position). This conformational change is considered as a first-order reaction with the rate μ_a . To model this process, let $p(s_2, t_2 | s_1, t_1)$ denote the probability density for a protein that desorbs at location s_1 at time t_1 to re-absorb at location s_2 at time t_2 .

This probability density can be calculated by considering the two stages of the protein desorption and re-absorption to the biopolymer. In the first stage, the protein desorbs at location s_1 along the biopolymer and performs three-dimensional diffusion until the occurrence of the conformational change at a time τ_a after desorption. At this

time the probability density the protein is at the location \mathbf{X} is given by $p_s(\mathbf{X} | s_1, \tau_a) = \frac{1}{(2\pi D\tau_a)^{3/2}} \exp \left[-\frac{(\mathbf{X} - \mathbf{Z}(s_1))^2}{4D\tau_a} \right]$, where $\mathbf{Z}(s_1)$ denotes the position on the biopolymer from which the protein desorbed and D the three-dimensional diffusion coefficient of the protein. In the second stage, the protein has affinity for the biopolymer and diffusively re-absorbs to the biopolymer at the location s_2 at time t_2 . We denote this probability density by $p_a(s_2, t_2 | \mathbf{X}, t_1 + \tau_a)$. This gives the density $p(s_2, t_2 | s_1, t_1) = \int_{\Omega} \int_0^{t_2-t_1} p_a(s_2, t_2 | \mathbf{x}, t_1 + t) p_s(\mathbf{x} | s_1, t) \mu_a e^{-\mu_a t} dt d\mathbf{x}$, which takes into account the role played by the geometry of the biopolymer conformation.

For simplicity we shall assume the biopolymer geometric conformation is fixed, resulting in a desorption and absorption process that is stationary. This gives $p_a(s_2, t_2 | s_1, t_1 + \tau_a) = p_a(s_2, t_2 - t_1 - \tau_a | s_1, 0)$. In practice, we tabulate $p_a(s_2, t | \mathbf{X}, 0)$ at select locations, \mathbf{X} , as a one-time off-line calculation using a numerical diffusion equation solver. This provides a very efficient method to simulate the excursions. To obtain τ_a , we first generate a random exponential time at which the affinity conformational change of the protein occurs. We then sample the protein location, $\mathbf{X} = \mathbf{x}$, using the density $p_s(\mathbf{X} | s_1, \tau_a)$. From our pre-constructed table, we can then sample $p_a(s_2, t_2 - t_1 - \tau_a | \mathbf{x})$ to find a time of re-absorption, t_2 , and the protein association location, s_2 . The protein will eventually be re-absorbed, because the three-dimensional spatial domain has reflecting boundaries and re-absorption to the polymer is modeled using a sink term which has support on a set of positive measure (see Subsection 7.2.2).

The modeled search process of the two proteins proceeds by drift-diffusion along the biopolymer and three-dimensional diffusive excursions until the proteins encounter each other on the polymer. The drift-diffusion along the biopolymer is handled by our one-dimensional DL-FPKMC algorithm with periodic boundary conditions. Upon a desorption event from location s_1 , the protein is repositioned on the biopolymer at location s_2 at the re-attachment time t_2 according to the density $p(s_2, t_2 | s_1, t_1)$. This repositioning process models the three-dimensional diffusive excursion of the protein until re-absorbing to biopolymer. We remark that reflecting boundary conditions or potential barriers in our DL-FPKMC method could be used to model obstructions on the biopolymer. Either potential sinks or absorbing Dirichlet boundary conditions could be used to model irreversible binding sites on the polymer.

7.2.2 Numerical Methods for Excursion-Time Probability Distribution and Reattachment Locations

We numerically solve the three-dimensional diffusion equation with diffusivity D for the position of a detached molecule at a given time. Denote by $\rho(\mathbf{x}, t)$ the corresponding probability density that solves the diffusion equation. Reattachment sites on a biopolymer are modeled using sink terms in the equation. We let s label the parameterization variable along the biopolymer, and s_0 the detachment position. From the probability mass absorbed at the locations of the sinks, we can obtain the probability densities $p(s, t | s_0, 0)$, where $p(s, t | s_0, 0)$ is as defined in the previous subsection. In the diffusion equation we use a sink term of the form

$$g(\mathbf{y}, t) = - \left(\int \lambda(s) q(\mathbf{y} - \mathbf{x}(s)) ds \right) \rho(\mathbf{y}, t),$$

where λ is the intensity of the sink and q is an averaging kernel function. The rate of the reattachment flux is given by

$$\frac{dQ}{dt}(s, t) = \int \frac{\lambda(s) q(\mathbf{y} - \mathbf{x}(s))}{\int \lambda(s') q(\mathbf{y} - \mathbf{x}(s')) ds'} g(\mathbf{y}, t) d\mathbf{y} = - \int \lambda(s) q(\mathbf{y} - \mathbf{x}(s)) \rho(\mathbf{y}, t) d\mathbf{y}.$$

In the discretized form this becomes

$$g(\mathbf{y}_m, t) = - \sum_k \lambda_k q(\mathbf{y}_m - \mathbf{x}(s_k)) \Delta s_k \rho(\mathbf{y}_m, t)$$

and the rate of the flux becomes

$$\frac{dQ_k(t)}{dt} = - \sum_m \lambda_k q(\mathbf{y}_m - \mathbf{x}_k) \Delta s_k \rho(\mathbf{y}_m, t) \Delta \mathbf{y}_m.$$

The particular choice that we make for the kernel q is the four-point Peskin- δ kernel [49]. For $\mathbf{x} = (x, y, z)$ this is given by $q(\mathbf{x}) = \phi_p(x/\Delta x) \phi_p(y/\Delta x) \phi_p(z/\Delta x)$, where

$$\phi_p(u) = \frac{1}{16} \begin{cases} 3 - 2u + \sqrt{1 + 4u - 4u^2} & 0 \leq u \leq 1, \\ 5 - 2u - \sqrt{-7 + 12u - 4u^2} & 1 \leq u \leq 2, \\ 0 & 2 \leq u, \end{cases}$$

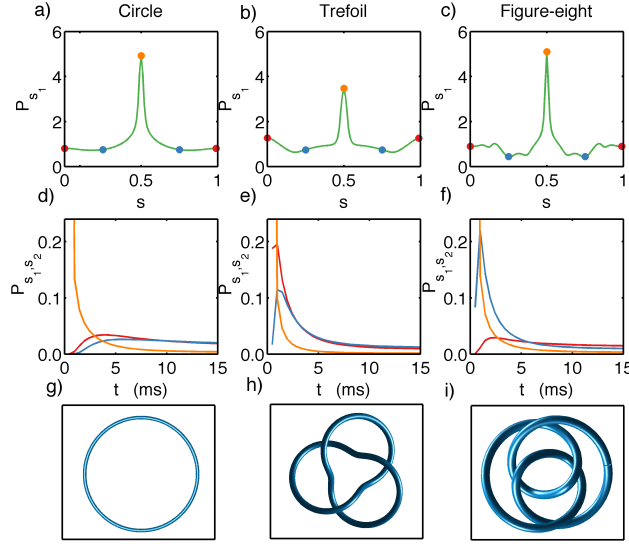


Figure 17: Reattachment probability distributions for the different topologies. (a–c) Probability density of absorbing at a given location $\mathbf{Z}(s)$ when the protein desorbed at location $\mathbf{Z}(0.5)$. $P_{s_1}(s) = \int_0^\infty p(s, t | s_1 = 0.5, 0) dt$. (d–f) Conditional probability densities for a protein that desorbed at location $\mathbf{Z}(0.5)$ to absorb at a point s_2 . For select locations these are indicated in the first row by a colored dot with the same color convention holding for the plots in the second row. $P_{s_1, s_2}(t) = p(s_2, t | s_1 = 0.5, 0)$. (g–i) Biopolymer geometries from left to right: a circular loop, trefoil knot, and figure-eight knot.

Table 2: Diffusion-excursion search parameters.

3D Parameters	Value	1D Parameters	Value
3D diffusion coefficient	$2.183823 \mu\text{m}^2\text{sec}^{-1}$	1D diffusion coefficient	$0.01 \mu\text{m}^2\text{sec}^{-1}$
μ_a	$5.1728 \times 10^7 \text{ns}^{-1}$	λ_{off}	0.02 to 200sec^{-1}
Δx	12.5nm	r_R	20 nm
Δt	4292.9ns	h_s^{max}	10 nm
$N_{\text{biopolymer}}$	100	h_p	5 nm
N_x, N_y, N_z	40	r_{pair}	$4 r_R = 80 \text{nm}$

with $\phi_p(-u) = \phi_p(u)$. This particular function is chosen to reduce numerical error induced by the off-lattice shifts of the polymer adsorption locations relative to the underlying discretization lattice used in the three-dimensional diffusion solver. We take the absorption parameter λ to have two stages. Namely, a “non-sticky” state $\lambda = 0$ and a “sticky” state $\lambda(s) = \lambda_k = \lambda_{\text{absorb}}$. The latter is taken to be uniform along the biopolymer. As discussed in Subsection 7.2.1, the protein becomes sticky after undergoing a conformational change, the time for which is modeled as an exponentially distributed random variable.

We consider three distinct geometric configurations for the biopolymer, each with the same arc-length but a different topology. Biopolymers represented by a circular unknotted loop, a trefoil knot, and a figure-eight knot are studied. We use parameterizations given by $X(s) = c * (x(s), y(s), z(s))$ for $0 \leq s \leq 1$, where c is chosen so that the arc-length of each of the knots is $L_{\text{biopolymer}} = 1000\text{nm}$. The x , y , and z parameterizations used for the three polymer configurations are: unknotted loop, $x(s) = \cos(2\pi s)$, $y(s) = \sin(2\pi s)$, $z(s) = 0$; trefoil knot, $x(s) = (2 + \cos(6\pi s)) \cos(4\pi s)$, $y(s) = (2 + \cos(6\pi s)) \sin(4\pi s)$, $z(s) = \sin(6\pi s)$; and figure-eight knot, $x(s) = (2 + \cos(4\pi s)) \cos(6\pi s)$, $y(s) = (2 + \cos(4\pi s)) \sin(6\pi s)$, $z(s) = \sin(8\pi s)$. For each configuration we use the diffusion equation solver to tabulate the joint reattachment time and location distribution (see Fig. 17). In the solver, the overall spatial domain containing the polymer is taken to be a box with sides of length 500nm.

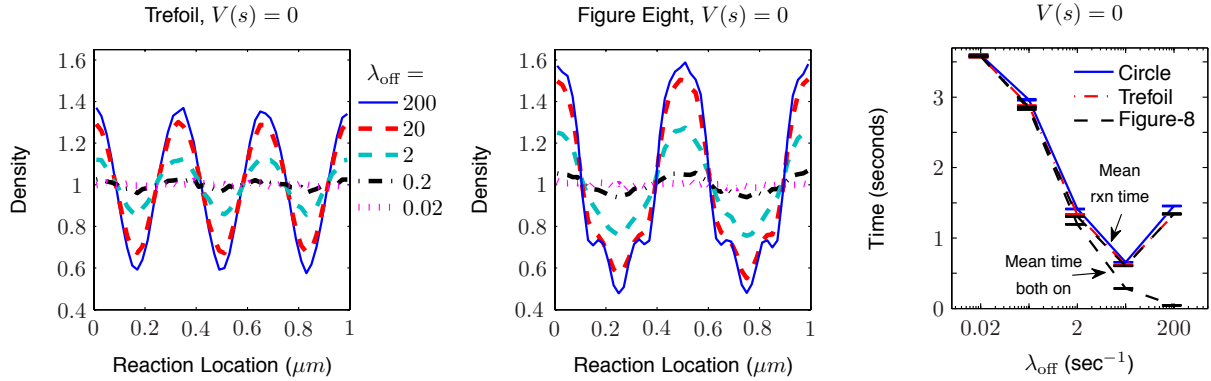


Figure 18: *Left and center panels:* Reaction location densities for $A + B \rightarrow \emptyset$ with $M^A(0) = M^B(0) = 1$ and $V(s) = 0$. The reaction location is the midpoint between the locations of A and B at the time of the reaction. Each graph is based on 10^6 simulations. The plotted densities were determined by binning the reaction locations into 50 bins. Note that no potentials are imposed in this figure. The non-uniformity in the reaction location density is a result of the polymer geometry. *Right panel:* Mean reaction time and mean time that both molecules are on the biopolymer. Each data point is based on 10^6 simulations. Error bars indicate 99% confidence intervals. The mean time that both molecules are on the biopolymer is shown for the figure-eight conformation only, but the results for the circle and trefoil conformations are similar.

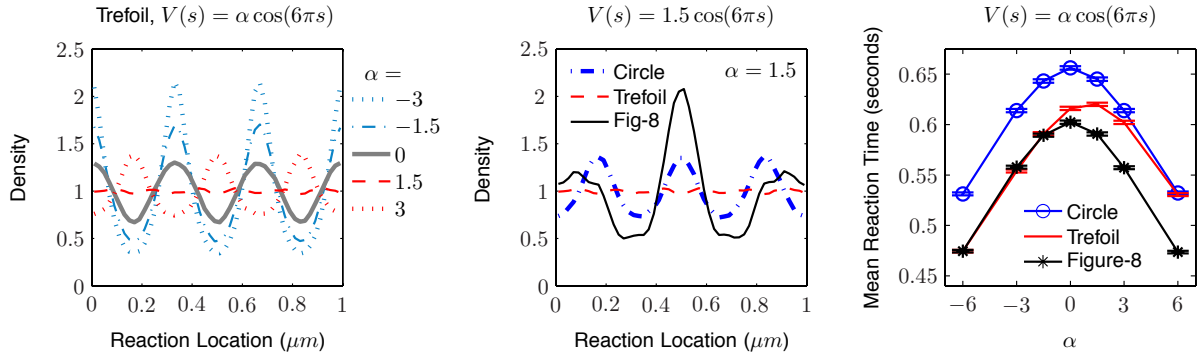


Figure 19: *Left and center panels:* Reaction location densities for $A + B \rightarrow \emptyset$, with $M^A(0) = M^B(0) = 1$, $V(s) = \alpha \cos(6\pi s)$, and $\lambda_{off} = 20 \text{ sec}^{-1}$. Each graph is based on 10^6 simulations. The plotted densities were determined by binning the reaction locations into 50 bins. *Right panel:* Mean reaction times. Each data point is based on 10^6 simulations. Error bars indicate 99% confidence intervals.

7.2.3 Simulation Results: Diffusion-Excursion Search with Different Biopolymer Geometries

We assume one molecule each of protein species A and B are initially present on the biopolymer. The initial positions are drawn from a uniform distribution over the length of the biopolymer. The two molecules undergo drift-diffusion along the biopolymer and diffusion in the three-dimensional space by the method developed in the preceding subsections. Detachment times are sampled from an exponential distribution with rate λ_{off} . A reaction between the two molecules can only occur when both are on the biopolymer.

For the parameters we take the three-dimensional diffusion coefficient to be $D = k_B T / \gamma$, where $\gamma = 6\pi\eta a$ is the Stokes drag, $a = 10$ nm is the radius of the protein, $T = 298.15$ is room temperature, k_B is Boltzmann constant, and the dynamic fluid viscosity, η , is chosen to be 10 times the viscosity of water. The parameter for the exponential distribution that represents when the protein becomes sticky is denoted by $\mu_a = 6D/r^2$, where $r = L_{\text{biopolymer}}/2\pi$. For convenience, the absorption strength, $\lambda_{\text{absorb}} = 0.005\text{ns}^{-1}$, is chosen to be larger than the timescale required for numerical stability in the diffusion equation solver. The other parameters are specified in Table 2.

For each biopolymer conformation, the reaction location distributions and the mean reaction times are investigated as the detachment rate, λ_{off} , is varied (Fig. 18). These simulations are for the case that $V(s) = 0$ along the polymer. As λ_{off} increases, the effects of the trefoil and figure-eight biopolymer geometries on the reaction locations become more pronounced (Fig. 18, left and center panels). For the unknotted circle the reaction locations are approximately uniform over the biopolymer regardless of the choice of λ_{off} . The mean reaction times attain a minimum at approximately $\lambda_{\text{off}} = 20$ and are slightly faster with the trefoil and figure-eight biopolymer conformations than with the circle conformation (Fig. 18, right panel). The mean total time that both molecules are on the biopolymer decreases monotonically as λ_{off} is increased (Fig. 18, right panel). Since the proteins spend more time diffusing in the three-dimensional space (off of the polymer) when λ_{off} is large, the polymer geometries affect the re-absorption locations more strongly (see Fig. 17), which in turn affects the reaction locations (Fig. 18).

A natural question is how diffusion in a potential energy landscape may enhance or counteract the effects of biopolymer geometry on the reaction locations. From Subsection 7.1, we expect the density of reaction locations to decrease in areas where the potential is large and to increase in areas where the potential is small. To test this idea, we investigated the trefoil knot conformation with potentials of the form $V(s) = \alpha \cos(6\pi s)$ for several values of $\alpha \in [-6, 6]$. The resulting reaction location densities as α is varied are shown in Figure 19 (left panel). As expected, the potential enhances the effects of the trefoil knot geometry when $\alpha < 0$, and counteracts the effects when $\alpha > 0$. When $\alpha = 1.5$, the effects of the potential and the trefoil geometry essentially cancel each other out. For comparison, we also ran simulations with $\alpha = 1.5$ for each of the other two biopolymer geometries (Fig. 19, center panel).

When the potential $V(s) = \alpha \cos(6\pi s)$ is used, the mean reaction time is fastest when the amplitude $|\alpha|$ is large (see Fig. 19, right panel). As discussed in Subsection 7.1, molecules that are in the same energy well of a potential tend to react more quickly. However, if the proteins can only move on the biopolymer, potentials with large amplitudes as used here would represent large energy barriers, greatly slowing the time for the two molecules to find each other. For example, with $\alpha = -3$ and $\lambda_{\text{off}} = 0$, the mean reaction time is approximately 80 ± 9 seconds, based on 10^3 simulations (compare to Fig. 19, right panel). The three-dimensional diffusion excursion provides an alternative path for proteins to circumvent the energy barriers present on the biopolymer. This could be an important mechanism in protein-protein interactions associated with biopolymers. As shown in Figure 19 (right panel), for the circle and figure-eight conformations, the maximum mean reaction time occurs when $\alpha = 0$, and the mean reaction times with positive and negative α of the same magnitude are similar. In contrast, for the trefoil conformation, the maximum mean reaction time occurs when $\alpha = 1.5$, which is the same value of α that resulted in the most uniform distribution of reaction locations (as was shown in Fig. 19, left panel). This demonstrates that the effect of the potential is not independent of the polymer geometry.

Overall, these results demonstrate the importance of incorporating drift-diffusion and other spatial heterogeneities, such as biopolymer geometry, when investigating biological chemical processes. They illustrate the power of the presented DL-FPKMC method in capturing such effects. Our approach and methods can be readily extended to more complex chemical kinetics, biopolymer geometries, or filament networks.

8 Conclusion

We have presented a new Dynamic Lattice First-Passage Kinetic Monte Carlo method (DL-FPKMC) that is capable of incorporating the roles played by drift and spatial heterogeneities into the stochastic dynamics of chemically reacting molecular species. We have shown that our numerical method is convergent for smooth potentials with approxi-

mately second-order accuracy and for discontinuous potentials with approximately first-order accuracy. Unlike the standard lattice RDME, our method retains bimolecular reactions as the lattice spacings within protective domains are taken to zero, and converges to the underlying SDLR model. In higher dimensions we expect the use of Walk on Rectangles [13] techniques will facilitate the incorporation of complex geometries into our method, while still allowing the use of basic Cartesian-grid meshes within each protective domain (hence avoiding the need for unstructured or embedded boundary meshes as commonly used for RDME models.)

We have further demonstrated how our method can be utilized in practice. In particular, the many examples we investigated demonstrate that drift can have a significant effect on reaction locations, reaction time distributions, and number of reactions that occur in a system. To demonstrate how our approach might be used for more complicated systems, we investigated the process of diffusion-excursion of proteins interacting with a biopolymer, taking into account geometric effects due to polymer shape. Such processes are thought to occur in the interactions between regulatory proteins and DNA. We considered a simplified model where the biopolymer has basic knotted configurations. Our results demonstrate that the combined effects of the biopolymer-protein interactions, biopolymer geometry, and drift-diffusion play a significant role in the chemical kinetics. The results also illustrate that capturing important features of biological systems may require models that account for drift-diffusion effects and spatial heterogeneities. We expect the DL-FPKMC methods we have introduced to be useful in performing more realistic simulations of the chemical kinetics of biological systems.

9 Acknowledgments

A.J.M. was supported by NSF DMS-0602204 EMSW21-RTG and Boston University. S.A.I. and A.J.M. were supported by NSF DMS-0920886 and NSF DMS-1255408. P.J.A. and J.K.S. were supported by NSF CAREER - 0956210. J.S. was supported by the CCS Summer Undergraduate Research Fellowship (SURF) program at UCSB and from P.J.A.’s startup funds (UCSB Math). The authors would like to thank the reviewers for their helpful comments and suggestions. In particular, Section 6 and Appendix A were added in response to reviewer comments.

A Constructing Protective Domains (PDs)

This appendix describes our method for constructing protective domains (PDs). It should be noted that this is just one of many possible approaches, and it is still an open question how best to optimize the partitioning of space among PDs. For the reader interested in this question we refer and defer to [17]. Regardless of the method used for constructing the PDs, our lattice approach of Section 4 can be used to propagate molecules within their respective PDs.

The PDs should be defined in a such a way that the distance between any two bimolecular reactants in separate PDs will remain strictly greater than their reaction radius, r_R , for as long as they remain in their respective PDs. This is necessary to ensure that the movements of molecules in separate PDs are independent. We allow the PDs of non-reacting molecules to overlap.

The following is the approach for defining PDs that resulted in the scaling demonstrated in Section 6. Steps 3 through 5 are specific to one dimension, but could be extended to higher dimensions by following a similar procedure in each coordinate. When constructing PDs for all molecules initially, or when updating the PDs of more than one molecule, we begin with the molecule closest to the left endpoint of the overall domain and then proceed to the right. An alternative approach would be to begin with a seed molecule and proceed outward.

1. For each molecule in need of a protective domain, identify the nearest potential reaction partners. In one dimension, this can be done by keeping a list of all molecules ordered by location. In higher dimensions, the near-neighbor list (NNL) method described in [17] can be used.
2. Determine which molecules will be placed in pair PDs. Two potential reaction partners are placed in a pair if:
 - the two molecules are closer to each other than to any other potential reaction partners, and
 - the distance between the two molecules is less than a pair threshold, r_{pair} , which is a parameter chosen by the user.

For the reaction system $A + B \rightarrow \emptyset$, we also enforce the condition in Eq. (20) when determining if two molecules will be placed in a pair. No other PDs are allowed to overlap with a pair PD.

3. For each molecule, identify its "limiting neighbor," which we define in the following way:

- For each molecule that will be in a pair PD, the limiting neighbor is the next nearest molecule of any type outside the pair.
- For a molecule that will be in a single PD, the limiting neighbor is the nearest molecule that is either a potential reaction partner or in a pair with another molecule.
- Let d_{nbr} be the distance from a molecule to its limiting neighbor. If a PD for the limiting neighbor has already been defined, let d_{nbrPD} be the distance from the molecule in question to the nearest endpoint of its limiting neighbor's PD.
- Note, a molecule is not necessarily the limiting neighbor of its limiting neighbor.

4. Determine the size of each pair PD and then the size of each single PD as follows, ignoring overall domain boundaries until Step 5:

- Pair PDs will be symmetric about the midpoint of the two molecules' locations. Single PDs will be symmetric about the location of the molecule.
- Let r_{PD} for a pair PD be the distance from either molecule to the nearest endpoint of the PD. For a single PD, r_{PD} will denote the distance from the molecule to either endpoint of the PD.
- Define Condition 1 to be that the limiting neighbor is a potential reaction partner, and Condition 2 to be that a PD for the limiting neighbor has not yet been defined.

For a single PD, calculate r_{PD} by

$$r_{\text{PD}} = \begin{cases} (d_{\text{nbr}} - r_{\text{R}})/2 & \text{if Conditions 1 and 2 hold} \\ d_{\text{nbrPD}} - r_{\text{R}} & \text{if only Condition 1 holds} \\ d_{\text{nbr}}/2 & \text{if only Condition 2 holds} \\ d_{\text{nbrPD}} & \text{otherwise.} \end{cases} \quad (21)$$

For a pair PD, calculate the quantity in Eq. (21) for each molecule and then set r_{PD} for the pair to be the minimum of the two quantities.

- We recommend capping the size of pair PDs, so that two molecules will not remain in a pair if they have moved sufficiently far away from each other. For example, r_{PD} for a pair PD could be set to the minimum of the value calculated above and half the initial distance between the two molecules in the pair.²
5. If a PD as defined in Step 4 extends beyond an endpoint of the overall domain, truncate the PD so that one endpoint of the PD will coincide with the overall domain endpoint. Such PDs will no longer be symmetric. An alternative approach would be to treat the overall domain boundary as a neighbor in Steps 1 through 4, and only allow a molecule's PD to touch the domain boundary if the distance to the boundary is less than r_{pair} .

B Derivation of Non-Uniform Jump Rates

To derive the non-uniform rates in Eq. (7), we use the fluxes from the WPE discretization [70]. As illustrated in Figure 3 (top row, left), $x_1 < x_0 < x_2$ are the locations of mesh points with non-uniform spacing $h_j = |x_0 - x_j|$. The jump rates a_{0j} from x_0 to x_j , $j = 1, 2$, are derived in this appendix. The solution $\rho(x, t)$ of the Fokker-Planck equation (4), gives the probability density of being at location x at time t . Let $\rho^{\text{eq}}(x)$ denote the equilibrium value of $\rho(x, t)$. Define $p_i(t)$ to be the probability of being at the mesh point x_i at time t in the discrete master equation model. We consider the point x_1 to represent the interval $(x_1 - \frac{h_1}{2}, x_1 + \frac{h_1}{2})$ in the sense that

$$p_1(t) \approx \int_{x_1 - \frac{h_1}{2}}^{x_1 + \frac{h_1}{2}} \rho(x, t) dx \approx \rho(x_1, t) h_1. \quad (22)$$

²The size of single PDs may be capped also. Generally speaking, the size of the PDs should be made as large as possible. However, making a particular molecule's PD as large as possible will result in less space for the PDs of neighbor molecules. Introducing a cap on the size of all PDs may result in a more equitable partitioning of space among them. We have not yet determined what value for the cap, if any, results in the most efficient performance of the overall algorithm. An optimal cap would mostly likely take into account the potential field (in DL-FPKMC), and would therefore vary spatially. See [17] for discussion of the case where different molecules have different diffusion coefficients in FPKMC.

Similarly, x_0 represents $(x_0 - \frac{h_1}{2}, x_0 + \frac{h_2}{2})$ and x_2 represents $(x_2 - \frac{h_2}{2}, x_2 + \frac{h_2}{2})$, so

$$p_0(t) \approx \rho(x_0, t) \frac{h_1 + h_2}{2} \quad \text{and} \quad p_2(t) \approx \rho(x_2, t) h_2. \quad (23)$$

Let $J(x, t)$ denote the flux

$$J(x, t) = -D \left(\rho(x, t) \frac{\partial V(x)}{\partial x} + \frac{\partial \rho(x, t)}{\partial x} \right).$$

For convenience, we define

$$A_{ik}(t) = \begin{cases} \frac{V(x_k) - V(x_i)}{\exp[V(x_k) - V(x_i)] - 1} & \text{for } V(x_k) \neq V(x_i) \\ 1 & \text{otherwise.} \end{cases}$$

Based on the WPE discretization, we approximate the unidirectional outward flux from x_0 to x_j by

$$J_{0j}(t) = \frac{D}{h_j} A_{0j}(t) \rho(x_0, t),$$

and the unidirectional inward flux from x_j to x_0 by

$$J_{j0}(t) = \frac{D}{h_j} A_{j0}(t) \rho(x_j, t).$$

Then, the net flux from x_0 to x_j is $J_{0j}(t) - J_{j0}(t)$. In the case that x_j , for $j = 1$ or 2 , lies on an absorbing Dirichlet boundary, $\rho(x_j, t) = 0$, and so we would have $J_{j0} = 0$ throughout the following calculation. The Fokker-Planck PDE (4) at x_0 is approximated by

$$\begin{aligned} \frac{\partial \rho(x_0, t)}{\partial t} &= -\frac{\partial}{\partial x} J(x_0, t) \approx \frac{2}{h_1 + h_2} \int_{x_0 - \frac{h_1}{2}}^{x_0 + \frac{h_2}{2}} -\frac{\partial}{\partial x} J(x, t) dx \\ &= \frac{2}{h_1 + h_2} \left(-J(x_0 + \frac{h_2}{2}, t) + J(x_0 - \frac{h_1}{2}, t) \right) \end{aligned} \quad (24)$$

$$\begin{aligned} &\approx \frac{2}{h_1 + h_2} ((J_{20} - J_{02}) - (J_{01} - J_{10})) \\ &= \frac{2}{h_1 + h_2} \left(\frac{D}{h_2} (A_{20} \rho(x_2, t) - A_{02} \rho(x_0, t)) - \frac{D}{h_1} (A_{01} \rho(x_0, t) - A_{10} \rho(x_1, t)) \right). \end{aligned} \quad (25)$$

When x_0 , x_1 , and x_2 are interior points, Taylor series expansion shows the spatial truncation error to be $O(h_1 - h_2)$ at x_0 . For $h_1 = h_2 = h$ the discretization is second-order accurate and we recover the WPE discretization. Note, as described in Section 4, we only use a non-uniform mesh for mesh cells bordering a boundary, or to move molecules onto a uniform mesh in a newly formed pair protective domain. When one of x_1 or x_2 corresponds to a (non-uniform) Dirichlet boundary point, and all interior mesh cells are uniform, the spatial discretization in Eq. (25) in the case that $V(x) = 0$ is known to be second-order accurate for the Poisson equation, see Ref. [25]. For a reflecting boundary at $x_0 - \frac{h_1}{2}$ or $x_0 + \frac{h_2}{2}$, the corresponding flux term in Eq. (24) is zero (since we assume reflecting boundaries are at the edges of mesh cells). The corresponding terms involving A_{0j} and A_{j0} then drop out of Eq. (25).

Multiplying Eq. (25) through by $\frac{h_1 + h_2}{2}$ and making the substitutions in Eqs. (22) and (23) yields the master equation

$$\frac{dp_0(t)}{dt} = \left(\frac{D}{h_2^2} A_{20} p_2(t) - \frac{2D}{h_2(h_1 + h_2)} A_{02} p_0(t) \right) - \left(\frac{2D}{h_1(h_1 + h_2)} A_{01} p_0(t) - \frac{D}{h_1^2} A_{10} p_1(t) \right).$$

Thus, we obtain the non-uniform jump rates (7)

$$a_{0j} = \frac{2D}{h_j(h_1 + h_2)} A_{0j} \quad j = 1, 2.$$

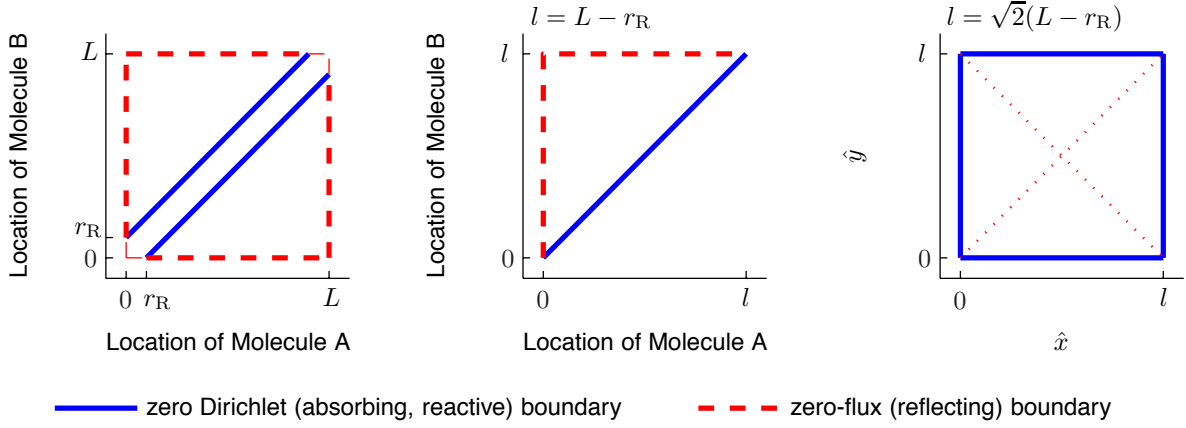


Figure 20: *Left*: 2D domain equivalent to 1D simulation domain of length L in which the two molecules are located. The zero Dirichlet boundaries on the diagonals correspond to the reaction occurring between the two molecules when they are one reaction radius apart. The zero-flux boundaries on the outer edges correspond to the reflecting endpoints of the 1D simulation domain. *Center*: PDE solver domain. *Right*: Eigenfunction expansion domain.

Whenever x_j is *not* a boundary point, the jump rate a_{j0} in the opposite direction agrees with the uniform rate in Eq. (5) with $h = h_j$. Hence, the system still satisfies a discrete detailed balanced condition at equilibrium (similar to the uniform WPE discretization):

$$a_{0j} \rho^{\text{eq}}(x_0) \frac{h_1 + h_2}{2} = a_{j0} \rho^{\text{eq}}(x_j) h_j,$$

since $\rho^{\text{eq}}(x)$ is given by the Gibbs-Boltzmann distribution $\rho^{\text{eq}}(x) \propto \exp[-V(x)]$ and

$$\frac{\rho^{\text{eq}}(x_j)}{\rho^{\text{eq}}(x_0)} = \frac{\exp[-V(x_j)]}{\exp[-V(x_0)]} = \frac{1}{\exp[V(x_j) - V(x_0)]}.$$

C Analytic and Numerical Solutions for the Two-Molecule Annihilation Reaction $A + B \rightarrow \emptyset$

In this Appendix we discuss the numerical solution of the Fokker-Planck equation and the analytic solution of the diffusion equation to which we compared the DL-FPKMC simulation results in Section 5.1. The 1D reaction-drift-diffusion system of two molecules undergoing the reaction $A + B \rightarrow \emptyset$ can be described by Eq. (9) on the 2D domain in the left panel of Figure 20. The solutions of the Fokker-Planck equation on the two disjoint triangular components of this domain are independent of each other. By symmetry, solving the Fokker-Planck equation on the domain in the left panel of Figure 20 can be reduced to solving the same equation on the single triangular domain in the center panel. We have written a PDE solver to solve the Fokker-Planck equation on the triangular domain. The PDE solver uses the rates in Eq. (5) from the WPE discretization [70] of the Fokker-Planck equation. This discretization is second-order accurate for smooth potentials and first-order accurate for discontinuous potentials. The mesh in the PDE solver is uniform.

The solution to the diffusion equation on the triangular domain in Figure 20 (center) can be recovered by solving on a square domain formed by adjoining four copies of the triangular domain at their reflecting (zero Neumann) edges, as shown in the right panel of Figure 20. On the square domain, an eigenfunction expansion for the solution can be determined analytically. This provides a check for the DL-FPKMC simulations in the $V = 0$ case, as well as a check for the PDE solver in that case. The solution $\rho(x, y, t)$ to the diffusion equation with constant initial condition

ρ_0 and diffusion coefficient D on a square domain with sides of length l is given by [51]:

$$\rho(x, y, t) = \frac{16\rho_0}{\pi^2} \left[\sum_{n=0}^{\infty} \frac{1}{2n+1} \sin\left(\frac{(2n+1)\pi x}{l}\right) \exp\left(\frac{-\pi^2(2n+1)^2 Dt}{l^2}\right) \right] \\ \times \left[\sum_{m=0}^{\infty} \frac{1}{2m+1} \sin\left(\frac{(2m+1)\pi y}{l}\right) \exp\left(\frac{-\pi^2(2m+1)^2 Dt}{l^2}\right) \right].$$

The survival probability $S(t)$, the probability that the two particles have not yet reacted by time t , is

$$S(t) = \int_0^l \int_0^l \rho(x, y, t) dx dy = \frac{64\rho_0 l^2}{\pi^4} \left[\sum_{n=0}^{\infty} \left(\frac{1}{2n+1}\right)^2 \exp\left(\frac{-\pi^2(2n+1)^2 Dt}{l^2}\right) \right]^2. \quad (26)$$

The mean reaction time is

$$\mathbb{E}[T] = - \int_0^{\infty} t S'(t) dt = \int_0^{\infty} S(t) dt = \frac{64\rho_0 l^4}{D \pi^6} \sum_{n=0}^{\infty} \sum_{m=0}^{\infty} \left(\frac{1}{2n+1}\right)^2 \left(\frac{1}{2m+1}\right)^2 \frac{1}{(2n+1)^2 + (2m+1)^2} \\ = \frac{16\rho_0 l^4}{D \pi^5} \sum_{n=0}^{\infty} \left(\frac{1}{2n+1}\right)^4 \left(\frac{\pi}{2} - \frac{\tanh(\frac{\pi}{2}(2n+1))}{(2n+1)}\right) \quad (27)$$

Evaluating $\mathbb{E}[T]$ at the parameter values corresponding to the two-molecule DL-FPKMC simulations in Section 5.1 gives a mean reaction time of 0.064831881311 seconds.

By symmetry the reaction location distribution can be calculated using the flux across any one of the four sides of the domain in Fig. 20 (right panel), since each side corresponds to a reactive boundary. Let $\boldsymbol{\eta} = \boldsymbol{\eta}(x, y)$ be the outward pointing normal at the point (x, y) . Using the boundary where $y = 0$, the reaction location distribution is

$$F^{\text{rxn}}(x) = 4 \int_0^x \int_0^{\infty} \left[-\frac{\partial}{\partial \boldsymbol{\eta}} \rho(\xi, y, t) \right]_{y=0} dt d\xi = 4 \int_0^x \int_0^{\infty} \left[\frac{\partial}{\partial y} \rho(\xi, y, t) \right]_{y=0} dt d\xi \quad (28) \\ = \frac{64\rho_0 l^2}{D \pi^4} \sum_{n=0}^{\infty} \sum_{m=0}^{\infty} \left(\frac{1}{2n+1}\right)^2 \frac{1}{(2n+1)^2 + (2m+1)^2} \left(1 - \cos\left(\frac{(2n+1)\pi x}{l}\right)\right) \\ = \frac{16\rho_0 l^2}{D \pi^3} \sum_{n=0}^{\infty} \left(\frac{1}{2n+1}\right)^3 \tanh\left(\frac{\pi(2n+1)}{2}\right) \left(1 - \cos\left(\frac{(2n+1)\pi x}{l}\right)\right).$$

For each of the potential functions, we ran the PDE solver using the Crank–Nicolson method in time, with spatial step sizes ranging from $\Delta x = r_R = 0.02$ to $\Delta x = r_R/16$ and time steps $\Delta t = \Delta x/16$. For $V = 0$, we can check the results of the PDE solver against the analytic solution; in this case, the numerical mean reaction times determined using the Crank–Nicolson method converge at approximately second-order ($m \approx 2.0025$) to the analytic mean reaction time. For $V \neq 0$, there is no analytic solution to which the numerical solutions can be compared; however, the decrease in the pairwise differences between the mean reaction times determined from the numerical PDE solutions at successive step sizes indicates convergence ($m \approx 1.9968$ for V_{cos} and $m \approx 0.9844$ for V_{step}). In the DL-FPKMC convergence results in Section 5.1, the empirical mean reaction times are compared to the analytic mean reaction time in the case $V = 0$, and to the numerical mean reaction times determined using the Crank–Nicolson PDE solver with the finest spatial step size, $\Delta x = r_R/16$, in the cases of V_{cos} and V_{step} .

The survival probabilities calculated using the Crank–Nicolson method show small numerical oscillations during the first few time steps. This is due to the incompatibility of the initial condition with the zero Dirichlet boundary condition. In order to numerically resolve the survival probabilities more accurately at short times, we re-ran the PDE solver using the Twizell–Gumel–Arigu (TGA) method [67] from $t = 0$ to $t = 0.07$ seconds. The TGA method is a second order, L_0 stable time discretization. We also used a finer time step, $\Delta t = (\Delta x)^2$ where $\Delta x = r_R/16$, to further improve the accuracy at short times when the survival probabilities change most rapidly. We then determined the numerical survival probabilities using the results from the TGA method for $t = 0$ to $t = 0.07$ seconds and using the results from Crank–Nicolson method for $t > 0.07$ seconds. At $t = 0.07$, the absolute difference in survival probabilities between the two methods is less than 10^{-8} for V_{cos} and less than 10^{-7} for V_{step} .

Table 3: Improved errors in numerical survival probabilities.

	Crank–Nicolson $\Delta x = r_R/16, \Delta t = \Delta x/16$	TGA $\Delta x = r_R/16, \Delta t = (\Delta x)^2$
L^1 Error	4.1117e-6	4.7909e-8
L^2 Error	8.2513e-5	1.6171e-6
L^∞ Error	5.8634e-3	2.2463e-4

To check that using the TGA method with a finer time step improved the accuracy of the numerical survival probabilities over the Crank–Nicolson method, we compared the numerical survival probabilities for $V = 0$ to the analytic survival probability on the interval from $t = 0$ to $t = 0.07$. Table 3 shows the absolute errors between the numerical survival probability calculated using each method and the analytic survival probability.

References

- [1] J. L. Adelman and S. S. Andrews. Intracellular pattern formation: A spatial stochastic model of bacterial division site selection proteins MinCDE. In *Proc. Santa Fe Inst. Summer School*, 2004.
- [2] B. Alberts, A. Johnson, J. Lewis, M. Raff, K. Roberts, and P. Walter. *Molecular Biology of the Cell*. Garland Science, New York, 5th edition, 2007.
- [3] S. S. Andrews, 2013. Publications using Smoldyn, see <http://www.smoldyn.org/publications.html>.
- [4] S. S. Andrews and D. Bray. Stochastic simulation of chemical reactions with spatial resolution and single molecule detail. *Physical Biology*, 1:137–151, 2004.
- [5] A. M. Arias and P. Hayward. Filtering transcriptional noise during development: concepts and mechanisms. *Nat. Rev. Genet.*, 7(1):34–44, 2006.
- [6] P. J. Atzberger and C. S. Peskin. A brownian dynamics model of kinesin in three dimensions incorporating the force-extension profile of the coiled-coil cargo tether. *Bulletin of Math. Biology*, 68(1):131–160, 2006.
- [7] B. Bayati, P. Chatelain, and P. Koumoutsakos. Adaptive mesh refinement for stochastic reaction-diffusion processes. *J. Comp. Phys.*, 230(1):13–26, 2011.
- [8] M. Beck, A. Schmidt, J. Malmstroem, M. Claassen, A. Ori, A. Szyborska, F. Herzog, O. Rinner, J. Ellenberg, and R. Aebersold. The quantitative proteome of a human cell line. *Molecular Systems Biology*, 7:1–8, November 2011.
- [9] O. G. Berg, R. B. Winter, and P. H. Von Hippel. Diffusion-driven mechanisms of protein translocation on nucleic acids. 1. models and theory. *Biochemistry*, 20(24):6929–6948, November 1981.
- [10] W. J. Blake, M. Kaern, C. R. Cantor, and J. J. Collins. Noise in eukaryotic gene expression. *Nature*, 422:633–637, April 2003.
- [11] A. B. Bortz, M. H. Kalos, and J. L. Lebowitz. A new algorithm for Monte Carlo simulation of Ising spin systems. *J. Comp. Phys.*, 17(1):10–18, 1975.
- [12] Y. Gao and L. Petzold. Accuracy limitations and the measurement of errors in the stochastic simulation of chemically reacting systems. *J. Comp. Phys.*, 212(1):6–24, February 2006.
- [13] M. Deaconu and A. Lejay. A random walk on rectangles algorithm. *Methodol. Comput. Appl. Probab.*, 8(1):135–151, Mar 2006.
- [14] M. Dobrzynski, J. V. Rodriguez, J. A. Kaandorp, and J. G. Blom. Computational methods for diffusion-influenced biochemical reactions. *Bioinformatics*, 23(15):1969–1977, May 2007.
- [15] M. Doi. Second quantization representation for classical many-particle system. *J. Phys. A: Math. Gen.*, 9(9):1465–1477, 1976.
- [16] M. Doi. Stochastic theory of diffusion-controlled reaction. *J. Phys. A: Math. Gen.*, 9(9):1479–1495, 1976.
- [17] A. Donev, V. V. Bulatov, T. Oppelstrup, G. H. Gilmer, B. Sadigh, and M. H. Kalos. A first-passage kinetic Monte Carlo algorithm for complex diffusion–reaction systems. *J. Comp. Phys.*, 229(9):3214–3236, January 2010.
- [18] J. Elf and M. Ehrenberg. Spontaneous separation of bi-stable biochemical systems into spatial domains of opposite phases. *IEE Sys. Biol.*, 1(2):230–236, December 2004.
- [19] M. B. Elowitz, A. J. Levine, E. D. Siggia, and P. S. Swain. Stochastic gene expression in a single cell. *Science*, 297:1183–1186, August 2002.
- [20] S. Engblom, L. Ferm, A. Hellander, and P. Lötstedt. Simulation of stochastic reaction-diffusion processes on unstructured meshes. *SIAM J. Sci. Comput.*, 31(3):1774–1797, 2009.

- [21] R. Erban and S. J. Chapman. Stochastic modelling of reaction-diffusion processes: algorithms for bimolecular reactions. *Phys. Biol.*, 6(4):046001, August 2009.
- [22] D. Fange, O. G. Berg, P. Sjöberg, and J. Elf. Stochastic reaction-diffusion kinetics in the microscopic limit. *PNAS*, 107(46):19820–19825, November 2010.
- [23] C. W. Gardiner. *Handbook of Stochastic Methods: For Physics, Chemistry, and the Natural Sciences*, volume 13 of *Springer Series in Synergetics*. Springer Verlag, New York, 2nd edition, 1996.
- [24] C. W. Gardiner, K. J. McNeil, D. F. Walls, and I. S. Matheson. Correlations in stochastic theories of chemical reactions. *J. Stat. Phys.*, 14:307–331, 1976.
- [25] F. Gibou, R. P. Fedkiw, L. Cheng, and M. Kang. A second-order-accurate symmetric discretization of the Poisson equation on irregular domains. *J. Comput. Phys.*, 176:205–227, 2002.
- [26] D. T. Gillespie. Exact stochastic simulation of coupled chemical-reactions. *J. Phys. Chem.*, 81(25):2340–2361, 1977.
- [27] J. Gorman and E. C. Greene. Visualizing one-dimensional diffusion of proteins along dna. *Nat Struct Mol Biol*, 15(8):768–774, August 2008.
- [28] S. Hellander, A. Hellander, and L. Petzold. Reaction-diffusion master equation in the microscopic limit. *Phys. Rev. E*, 85(4):042901(1–5), April 2012.
- [29] S. Hellander and P. Lötstedt. Flexible single molecule simulation of reaction-diffusion processes. *J. Comput. Phys.*, 230:3948–3965, May 2011.
- [30] T. Hu, A. Y. Grosberg, and B. I. Shklovskii. How proteins search for their specific sites on dna: The role of dna conformation. *Biophysical Journal*, 90(8):2731–2744, April 2006.
- [31] S. A. Isaacson. Relationship between the reaction-diffusion master equation and particle tracking models. *J. Phys. A: Math. Theor.*, 41(6):065003 (15pp), 2008.
- [32] S. A. Isaacson. The reaction-diffusion master equation as an asymptotic approximation of diffusion to a small target. *SIAM J. Appl. Math.*, 70(1):77–111, 2009.
- [33] S. A. Isaacson. A convergent reaction-diffusion master equation. *J. Chem. Phys.*, 139(5):054101, 2013.
- [34] S. A. Isaacson and D. Isaacson. Reaction-diffusion master equation, diffusion-limited reactions, and singular potentials. *Phys. Rev. E*, 80(6):066106 (9pp), 2009.
- [35] S. A. Isaacson, D. M. McQueen, and C. S. Peskin. The influence of volume exclusion by chromatin on the time required to find specific DNA binding sites by diffusion. *PNAS*, 108(9):3815–3820, March 2011.
- [36] S. A. Isaacson and C. S. Peskin. Incorporating diffusion in complex geometries into stochastic chemical kinetics simulations. *SIAM J. Sci. Comput.*, 28(1):47–74, 2006.
- [37] J. Keizer. Nonequilibrium statistical thermodynamics and the effect of diffusion on chemical reaction rates. *J. Phys. Chem.*, 86:5052–5067, 1982.
- [38] B. N. Kholodenko, J. F. Hancock, and W. Kolch. Signalling ballet in space and time. *Nat Rev Mol Cell Biol*, 11:414–426, June 2010.
- [39] S. Kullback and R. A. Leibler. On information and sufficiency. *Ann. Math. Statist.*, 22(1):79–86, 1951.
- [40] J. Lipkova, K. C. Zygalkis, S. J. Chapman, and R. Erban. Analysis of Brownian Dynamics simulations of reversible bimolecular reactions. *SIAM J. Appl. Math.*, 71(3):714, 2011.
- [41] C. Loverdo, O. Benichou, M. Moreau, and R. Voituriez. Enhanced reaction kinetics in biological cells. *Nat. Phys.*, 4:134–137, 2008.
- [42] H. Maamar, A. Raj, and D. Dubnau. Noise in gene expression determines cell fate in *Bacillus Subtilis*. *Science*, 317:526–529, July 2007.
- [43] D. A. McQuarrie. Stochastic approach to chemical kinetics. *J. Appl. Prob.*, 4:413–478, 1967.
- [44] L. Mirny, M. Slutsky, Z. Wunderlich, A. Tafvizi, J. Leith, and A. Kosmrlj. How a protein searches for its site on DNA: the mechanism of facilitated diffusion. *J. Phys. A: Math. Theor.*, 42(43):434013, Jan 2009.
- [45] M. E. Muller. Some continuous Monte Carlo methods for the Dirichlet problem. *Ann. Math. Statistics*, 27:569–589, 1956.
- [46] J. Muñoz-García, Z. Neufeld, B. N. Kholodenko, and H. M. Sauro. Positional information generated by spatially distributed signaling cascades. *PLoS Comp. Biol.*, 5(3):e1000330, March 2009.
- [47] T. Oppelstrup, V. V. Bulatov, A. Donev, M. H. Kalos, G. H. Gilmer, and B. Sadigh. First-passage kinetic Monte Carlo method. *Phys. Rev. E*, 80(6):066701, December 2009.
- [48] T. Oppelstrup, V. V. Bulatov, G. H. Gilmer, M. H. Kalos, and B. Sadigh. First-passage Monte Carlo algorithm: Diffusion without all the hops. *Phys. Rev. Lett.*, 97(23):230602, Dec 2006.
- [49] C. S. Peskin. The immersed boundary method. *Acta Numerica*, 11:479–517, 2002.
- [50] C. S. Peskin and G. Oster. Coordinated hydrolysis explains the mechanical behavior of kinesin. *Biophys. J.*, 68(4 Suppl):202S, 1995.
- [51] A. D. Polyanin. *Handbook of Linear Partial Differential Equations for Engineers and Scientists*. Chapman & Hall/CRC, 2002.
- [52] A. Raj, C. S. Peskin, D. Tranchina, D. Y. Vargas, and S. Tyagi. Stochastic mRNA synthesis in mammalian cells. *PLoS Biology*, 4(10):e309, 2006.
- [53] R. Ramaswamy, N. Gonzalez-Segredo, I. F. Sbalzarini, and G. Ramon. Discreteness-induced concentration inversion in

- mesoscopic chemical systems. *Nat. Commun.*, 3:779 (8pp), 2012.
- [54] R. Ramaswamy and I. F. Sbalzarini. Exact on-lattice stochastic reaction-diffusion simulations using partial-propensity methods. *J. Chem. Phys.*, 135:244103 (17pp), 2011.
 - [55] J. Raser and E. O'Shea. Control of stochasticity in eukaryotic gene expression. *Science*, 304:1811–1814, Jan 2004.
 - [56] A. D. Riggs, S. Bourgeois, and M. Cohn. The lac repressor-operator interaction: Iii. kinetic studies. *Journal of Molecular Biology*, 53(3):401–417, November 1970.
 - [57] D. Rossinelli, D. Bayati, and P. Koumoutsakos. Accelerated stochastic and hybrid methods for spatial simulations of reaction-diffusion systems. *Chemical Physics Letters*, 451(1–3):136–140, 2008.
 - [58] K. Schwarz and H. Rieger. Efficient kinetic monte carlo method for reaction-diffusion problems with spatially varying annihilation rates. *J. Comp. Phys.*, 237:396–410, 2013.
 - [59] N. Shimamoto. One-dimensional diffusion of proteins along dna. *Journal of Biological Chemistry*, 274(22):15293–15296, May 1999.
 - [60] M. Slutsky and L. A. Mirny. Kinetics of protein-DNA interaction: facilitated target location in sequence-dependent potential. *Biophys. J.*, 87(6):4021–35, Dec 2004.
 - [61] M. V. Smoluchowski. Mathematical theory of the kinetics of the coagulation of colloidal solutions. *Z. Phys. Chem.*, 92:129–168, 1917.
 - [62] T. Sokolowski, L. Bossen, T. Miedema, and N. Becker. Green's function reaction dynamics—an exact and efficient way to simulate intracellular pattern formation. In T. E. Simos, G. Psihoyios, and Ch. Tsitouras, editors, *ICNAAM, Numerical Analysis and Applied Mathematics, International Conference 2010, Vol. II*, volume 1281 of *AIP Conf. Proc.*, pages 1342–1345, 2010.
 - [63] V. Sourjik and N. S. Wingreen. Responding to chemical gradients: bacterial chemotaxis. *Current Opinion in Cell Biology*, 24(2):262–268, April 2012.
 - [64] G. M. Süel, J. G. Garcia-Ojalvo, L. M. Liberman, and M. B. Elowitz. An excitable gene regulatory circuit induces transient cellular differentiation. *Nature*, 440:545–550, March 2005.
 - [65] K. Takahashi, S. Tanase-Nicola, and P. R. ten Wolde. Spatio-temporal correlations can drastically change the response of a MAPK pathway. *PNAS*, 107(6):2473–2478, February 2010.
 - [66] E. Teramoto and N. Shigesada. Theory of bimolecular reaction processes in liquids. *Prog. Theor. Phys.*, 37(1):29–51, 1967.
 - [67] E. H. Twizell, A. B. Gumel, and M. A. Arigu. Second-order, L_0 -stable methods for the heat equation with time-dependent boundary conditions. *Advances in Computational Mathematics*, 6(3):333–352, 1996.
 - [68] N. G. Van Kampen. *Stochastic Processes in Physics and Chemistry*. North-Holland, Amsterdam, 2001.
 - [69] J. S. van Zon and P. R. ten Wolde. Simulating biochemical networks at the particle level and in time and space: Green's function reaction dynamics. *Physical Review Letters*, 94(12):128103, 2005.
 - [70] H. Wang, C. S. Peskin, and T. C. Elston. A robust numerical algorithm for studying biomolecular transport processes. *J. Theor. Biol.*, 221:491–511, 2003.
 - [71] Y. M. Wang, R. H. Austin, and E. C. Cox. Single molecule measurements of repressor protein 1d diffusion on dna. *Phys. Rev. Lett.*, 97(4):048302, July 2006.